NO VTT-R-10851-07| 13.3.2008

FP6-036367 ANTIOXI

ANTIOXI -Incorporation of coolant originating cations into the oxide films on stainless steels - experiments and modelling

Authors: Martin Bojinov, Petri Kinnunen, Markus Olin

Confidentiality: Public

Report's title	
ANTIOXI - Incorporation of coolant originating cations into the oxide films on stainless steels - experiments and modelling	
Customer, contact person, address EC / Marc Deffrennes, Commission européenne, Rue du Champ de Mars 21, B- 1050 Brussels, Belgium	Order reference
Project name ANTIOXI	Project number/Short name 6402 ANTIOXI
Author(s) Martin Bojinov, Petri Kinnunen, Markus Olin	Pages 39
Keywords oxide film, hematite, magnetite Zn, PWR, stainless steel, sorption	Report identification code VTT-R-10851-07

Summary

The oxidation of AISI 316L(NG) stainless steel in simulated Pressurised Water Reactor (PWR) coolant with or without addition of 1 ppm Zn at 280°C for up to 96 h has been characterised in-situ by Electrochemical Impedance Spectroscopy (EIS). Additional tests were performed in simulated PWR coolant with the addition of 0.01 M $Na_2B_4O_7$ to exclude the effect of pH excursions probably due to Zn hydrolysis reactions. The thickness and in-depth composition of the oxide films formed at open circuit and at 0.5 V vs. RHE in the investigated electrolytes have been estimated from X-ray photoelectron spectroscopy (XPS) depth profiles. The kinetic and transport parameters characterising the oxide layer growth have been estimated using a calculation procedure based on the Mixed Conduction Model for oxide films. Successful simulations of both the EIS and XPS data have been obtained using the proposed procedure. The parameter estimates are discussed in terms of the effect of Zn on the growth and restructuring of the oxide layers on stainless steel in LWR conditions.

In addition, sorption tests were employed to quantitatively estimate the adsorption of a range of aquoions (Co, Ni, Zn, and Sb) on hematite and magnetite type oxides. This was accomplished by measuring the solution concentrations before and after the sorption. Some data on the kinetics of sorption of Sb have been also obtained. The surface site density on both oxides was determined by the Gran method both at ambient temperature and at 280 °C. The results were interpreted by using the 1-pK approach of the surface complexation model, and the electrostatic effects were taken into account by employing a constant capacitance or diffuse layer models. Stability constants of surface complexes of Co, Ni, Zn and Sb on magnetite and hematite oxides have been estimated and discussed.

Confidentiality	Public

Espoo 12.3.2008

Signatures	Signatures
Accepted by Liisa Heikinheimo Technology Manager	Written by Petri Kinnunen, Senior Research Scientist, Coordinator

VTT's contact address
P.O.Box 1000, 02044 VTT, Finland

Distribution (customer and VTT)

European Commission 1 original
VTT 1 original
BGH2 Society 1 original

Preface

The work discussed in the present report has been carried out as in the Work Package 2 of the project FP6-036367 A deterministic model for corrosion and activity incorporation in nuclear power plants (ANTIOXI) in 2006 - 2007. The ANTIOXI project is a part of the EURATOM FP6 Programme “Advanced tools for nuclear safety assessment and component design”.

The ANTIOXI project in EURATOM FP6 concentrates on development of modelling tools for activity incorporation and corrosion phenomena into oxide films on construction materials in light water reactor environments.

The main funding source of the work has been the Sixth Framework Programme of the European Commission. The cooperation of the Members of the Advisory Board of the ANTIOXI project is gratefully acknowledged.

Espoo, Finland, March 12th 2008

Authors

Contents

1 Introduction

The objective of the ANTIOXI project is to develop a deterministic model for the build-up and properties of the oxide layers formed on LWR out-of-core primary system surfaces. The main focus in the development is to be able to model and predict the radioactivity build-up occurring on these surfaces. The work done in the work package 2 (WP 2) of the ANTIOXI project and described in this report includes two different experimental approach to study the effects of electrolyte originating species on the surfaces of stainless steels.

The first approach selected was to study electrochemically and with ex-situ analytical techniques the incorporation of electrolyte originating species such as Zn into the oxide film formed on AISI 316 stainless steel in buffered and unbuffered simulated Pressurised Water Reactor (PWR) conditions at 280°C. Also the effect of this process on film growth and restructuring was included in the study. The modelling of these features is based on the Mixed-Conduction Model for Oxide Films (MCM). Calculation procedures based on a quantitative comparison of the model equations to in-situ electrochemical impedance spectroscopic (EIS) data and ex-situ the X-ray photoelectron spectroscopic (XPS) in-depth concentration profiles of the constituent elements were employed. The experimental data are presented and qualitatively discussed in terms of the effect of Zn addition on both the conduction mechanism and the in-depth composition of the oxide layers. The model concepts and the calculational procedure are briefly introduced emphasizing the simplifying assumptions made and thus both the abilities and the limitations of such a procedure. Calculational results are presented and discussed in terms of different hypotheses for the effect of Zn on the growth and restructuring of the oxide layer on stainless steel during the initial stages of exposure to PWR water. The validation of this method has been performed recently using measurement results for AISI 304 stainless steel after a prolonged exposure to simulated PWR water with or without zinc addition and comparing them with the recent literature data [1].

The second approach was to study the sorption of different cations onto the hematite and magnetite surfaces. Based on the results the aim was to estimate the equilibrium constants and further the concentrations of adsorbed species at the very first stage of interaction between the cation and the surface. The experiments were conducted so that the surface re-precipitation could be avoided. Quantification of the surface complexation / deposition constants through high-temperature laboratory measurements was made by using the 1-pK approach to a surface complexation model and treating the surface charge – surface potential relationship in terms of different electrostatic models.

2 Goal

The goal of the present work is to compare quantitatively the predictions of the MCM to both in-situ EIS and ex-situ XPS data for oxides on AISI 316L(NG) formed for up to 4 days in simulated PWR water at 280°C with or without Zn addition. Also, we aim at quantitative modelling of the mechanism of sorption of cations on magnetite and hematite surface using the 1-pK approach of the surface complexation model.

3 Description

First, the experimental data for oxides on AISI 316L(NG) formed for up to 4 days in simulated PWR water at 280°C with or without Zn addition are presented and qualitatively discussed in terms of the effect of Zn addition on both the conduction mechanism and the in-depth composition of the oxide layers. Second, the model concepts and the calculation procedure are

briefly introduced emphasizing the simplifying assumptions made and thus both the abilities and the limitations of such a procedure. Third, calculation results are presented and discussed in terms of different hypotheses for the effect of Zn on the growth and restructuring of the oxide layer on stainless steel during the initial stages of exposure to PWR water.

For the studies concerning the sorption of cations on hematite and magnetite surfaces, the experimental approach to evaluate the surface properties of these oxides is described. Then the calculation procedure to estimate surface site concentrations is given. After this the results obtained from the batch experiments and the surface complexation analysis in the relevant environments is shown and explained.

4 Limitations

In the sorption tests one of the most crucial limitations was the analysis of the solution samples. The analyses were bought from Loviisa NPP's chemistry laboratory and the number of samples that could be analysed there was limited. Therefore not a large sample matrix was analysed. Another limitation that became important for this project was that a replacement for the person able to model the surface properties of the studied oxides was performed during the project. This replacement lengthened the time needed for the work to some extent.

5 Experimental

5.1 EIS studies on Zn incorporation

Incorporation of Zn was studied using a static PTFE lined autoclave. The working electrodes were manufactured from AISI 316 L(NG) stainless steel. PTFE-insulated rectangular samples with a working area of 6.3 cm^2 were used for both the impedance measurements and the exposure aimed at a subsequent ex-situ XPS characterisation. The working electrode pretreatment consisted of mechanical polishing with emery paper up to grade 4000 and rinsing with ultrapure water (resistivity > 18 MΩ cm). Temperature in all tests was 280±2°C and the corresponding pressure ca. 9-9.5 MPa. A Pt sheet was used as a counter electrode. All potentials were measured vs. a Pd electrode electrochemically charged with hydrogen to approximate the reversible hydrogen electrode (RHE). The used charging current was 70µA.

A total of four samples were used in every test: two samples for impedance measurements and two for ex situ analysis. One EIS and one ex-situ analysis sample were polarised during the tests while the other two were held at open circuit potential. The polarisation of the impedance sample was started after one day oxidation at open circuit at the test temperature. The polarisation was performed with 100mV steps starting from 0 V up to 0.5 V vs. RHE and. The polarisation time was 30 minutes at each potential after which an impedance spectrum was measured. The ex-situ sample was polarised at 0.5 V vs. RHE starting after one day oxidation at open circuit at the test temperature. The duration of the whole test run was ca. four days.

The electrolyte was simulated PWR coolant (1200 ppm B as H_3BO_3, 2.2 ppm Li as LiOH) with or without the addition of 1 ppm Zn as $Zn(NO_3)_2$ and/or 0.01 M $Na_2B_4O_7$ which was added to buffer the electrolyte and prevent any pH excursions due to hydrolysis reactions of soluble Zn. The measurements were performed under slow continuous bubbling with N_2 (99.999%). According to earlier experience, a conservative estimate of the maximum hydrogen level in such conditions at high temperatures is ca. 600 ppb (10 cm^3 kg^{-1} at a standard temperature and pressure) and the maximum oxygen level is ca. 10-20 ppb (3-7 × 10^{-7} mol dm^{-3}).

Impedance spectra in the alloy/oxide/electrolyte configuration were obtained with a PAR 283 /5210 system controlled by PowerSine software (Princeton Applied Research) in a frequency range of 80 kHz down to 0.1 mHz at an ac signal amplitude of 50 mV(rms). The validation of the impedance spectra was performed by checking the linearity condition, i.e. measuring spectra at different signal amplitudes. The spectra were also found to be compatible with the Kramers-Kronig transforms within the experimental error (±2% by magnitude and ±4º by phase angle).. For the simulation and fitting of impedance spectra to the transfer function derived from the kinetic model, Origin 7.5-based software routines have been employed.

XPS spectra were registered using an ESCALAB Mk II (VG Scientific) electron spectrometer with a base pressure of $\approx 10^{-7}$ Pa. The photoelectrons were excited with a Mg Kα (1253.6 eV) X-ray source and the analyzer pass energy was 20 eV. The B1s, C1s, O1s, Fe2p, Cr2p, Ni2p and Zn2p photoelectron lines were recorded and the binding energies were calibrated versus the C1s peak. To obtain depth profiles, Ar ion milling was used and the conversion of the sputtering time to depth has been performed with respect to a Ta_2O_5 standard (sputtering rate 0.4 nm min^{-1}). The peak positions were determined by Gaussian-Lorentzian peak fitting after Savitzky-Golay smoothing and Shirley background subtraction, and peak areas were converted to atomic concentrations as depending on sputtering depth. The position of the metal/oxide interface has been estimated using sigmoidal fitting of the oxygen profiles in order to locate their inflection point situated at 50% of the atomic concentration of oxygen at the oxide surface. Another estimate of the position of the metal/oxide interface was provided by the depth at which the concentration of metallic Cr equals that of Cr(III) [11]. The boundary between the inner and outer layers was estimated by sigmoidal fitting of the respective profiles of the main element, Fe. The concentrations of the metallic constituents of the oxide were converted to mass fractions by normalising them with the total concentration of metallic constituents. For the simulation of the depth profiles of the mass fractions of the metallic elements according to the MCM, the respective non-steady state differential equations were solved using Maple 8.1 software [1].

5.2 Sorption and titration experiments

In the sorption tests the goal was find how much different cations are adsorbed on hematite and magnetite type oxides. This information could be obtained by studying solution concentrations before and after the sorption. The experiments were performed in the same static autoclave as the EIS experiments described above. The tests were made as batch experiments the duration of one test being ca. five hours (including heating of the autoclave). A scheme of the used equipment is shown in Figure 1.

In the beginning of a sorption test a suspension containing either 50 g of hematite Fe_2O_3 (99.7%, PROLABO) or 10 g magnetite (98%, Alfa Aesar) in 1000 ml of simulated “PWR water” with $Na_2B_4O_7$ was added to the autoclave, de-aerated with N_2 (99.999%)gas (AGA) and heated up to 280°C. The difference in the amounts of different oxide powders used is due to different measured surface site densities (see below the determination of surface site density): 7.5×10^{-7} mol g^{-1} for Fe_2O_3 and 7×10^{-5} mol g^{-1} for Fe_3O_4. The used “PWR water” composition was 3.81 g l^{-1} $Na_2B_4O_7$, 6.87 g l^{-1} H_3BO_3 and 7.54 mg l^{-1} LiOH. Sodium tetraborate was added to solution to prevent any pH excursions. After reaching the test temperature and pressure, continuous N_2 bubbling was started and solution containing the specific cation of interest was pumped in. After 5, 15 and 30 minutes hot samples were taken from the autoclave via the sampling line. A 15 micron particle filter was added to the sampling line to remove any solid oxides possibly coming out from the autoclave during sampling. The used cation solutions were 0.005 M $Ni(NO_3)_2 \times 6H_2O$ (Merck), 0.005 M $Co(NO_3)_2 \times 6H_2O$ (Merck) and 0.005 M $Zn(NO_3)_2 \times 6H_2O$ (Merck). Sb was added as 1mg/ml + 2.5% HCl solution (Spectrascan) due to the fact that Sb is very difficult

to obtain in “pure” solution. The starting concentration in the solution for each cation was selected to be 1 ppm.

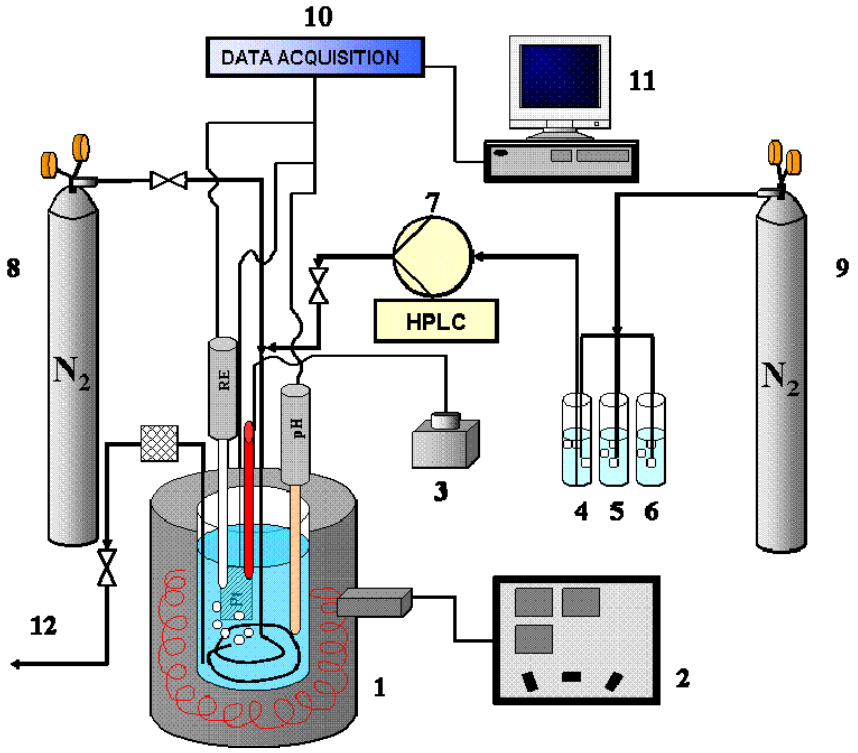

Figure 1. A scheme of the equipment used for sorption experiments and high temperature titrations. 1*: high-temperature autoclave including a PTFE vessel, reference, counter and pH electrodes, a heating cartridge for the solution inside the PTFE vessel, a pipe used to feed more solution into the autoclave and to degas the solution and a thermocouple sensor for monitoring temperature,* 2*: control unit for the autoclave,* 3*: control unit for the heating cartridge in the PTFE vessel,* 4-6*: solutions containing the studied cations, acid or base solutions and water to flush the pipe line,* 7*: high-pressure liquid chromatography pump to add solutions to the autoclave,* 8*: nitrogen bubbling to remove oxygen from the autoclave,* 9*: nitrogen to remove oxygen from the solutions to be added to the autoclave,* 10*: data acquisition equipment,* 11*: computer,* 12*: sampling line including a particle filter for high temperature samples to be taken during the experiments.*

The hot samples collected from the autoclave were acidified with 1 ml of 65% Suprapur HNO_3 (Merck) to prevent the adsorption of solution species to the bottle wall. The analysis of the samples was performed at Fortum Loviisa NPP chemistry laboratory. The analyses were performed with an electrothermic atomic absorption spectrometer Perkin Elmer SIMAA 6100 based on the anlysis instruction K-14-00005. For the analysis the samples were diluted to 10/20 mL+0.1 mL HNO_3.

In order to be able analyse the sorption behaviour in more details the surface site concentration for each used oxide needed to be determined. The specific area of the oxides has to be first known. This analysis has been performed by using nitrogen adsorption (Flowsorb, N2:He = 30:70, GTK Outokumpu).The specific surface area for hematite was found to be 8.3 $m^2\ g^{-1}$ [2] and for magnetite 39.8 $m^2\ g^{-1}$.

As the hematite surface properties had been studied already earlier [2] in this project the surface site density was determined only for magnetite. The actual determination of surface sites analysis can be made with both ambient and high temperature titration and the analytical approach by

Gran [3]. At high temperatures the titrated solution consisted of purified water the H^+ concentration of which was adjusted to 0.0034 M with 1 M HNO_3 (Merck) and the studied oxide powder. Prior the titration the autoclave was heated up with only 1500 ml purified water in the PTFE vessel. When the temperature of the solution in the PTFE vessel reached 280°C, a volume of 50 ml of solution containing 5.5 ml 1 M HNO_3 and 50 ml of water was pumped in the vessel. In theory (and also in practise) this acid addition should result to high-temperature pH of 2.4…2.5. The reason for pumping the solutions in the vessel in this manner and the acidification of the solution just before the titration was to avoid the decomposition of nitric acid during the heat-up period of the autoclave. Furthermore, the metallic surfaces in contact with the acidified solution were coated with PTFE tape as completely as possible to minimise the decomposition of acid on these surfaces.

The used titrant was 0.1 M NaOH (Merck) and it was dosed by a high-pressure liquid chromatography (HPLC) pump with a flow rate of 1 ml/min. The mixing of the solutions inside the PTFE vessel was carried out by nitrogen bubbling (AGA 5.0, 99.999% N_2) through a metal spiral installed at the bottom of the vessel. The same arrangement was also used to deoxygenate the pumped solutions and for the pressure adjustment.

The pH during the titration was measured with an oxygen-ion-conducting ceramic membrane sensor based on yttrium stabilised zirconium oxide, ZrO_2 (Y_2O_3), and an internal reference couple, which was Cu_2O/Cu. A silver–silver chloride electrode filled with 0.1 M KCl was used as the reference electrode. All the potentials were measured versus the body of the Ti-clad autoclave. Potential values of the electrodes were registered using computer controlled data acquisition equipment (Agilent). The sensors employed in the measurements are specially designed and manufactured at VTT.

The titrations at ambient measurements were conducted in a similar fashion but with smaller volumes and in a glass vessel. The pH was monitored with a commercial glass electrode (Contronic). The titration was performed by adding 0.1 M NaOH with the rate 0.2 $mlmin^{-1}$

6 Results

6.1 Incorporation of Zn in the oxide film on AISI 316 in simulated PWR coolant

6.1.1 Electrochemical impedance spectroscopy

Impedance spectra for AISI 316L(NG) stainless steel in simulated PWR coolant at a range of potentials (0 – 0.5 V vs. RHE) after a 48 h exposure at 280°C without and with the addition of 1 ppm Zn are presented in Figure 2a-b. The corresponding spectra in PWR water with the addition of 0.01 M $Na_2B_4O_7$ are shown in Figure 3a-b, respectively. It is worth mentioning that the oxide layers were allowed to form at open circuit for 24 h before any Zn was injected into the electrolyte. Subsequently, the films were allowed to grow for another 24 h period before measuring the impedance spectra as a function of potential. The conductivity of the electrolyte with 0.01 M $Na_2B_4O_7$ addition was substantially higher than that of the plain simulated PWR water. Therefore, the electrolyte resistance estimated from the high-frequency intercept of the impedance spectra has been subtracted from the data in order to facilitate the comparison between spectra in the two electrolytes.

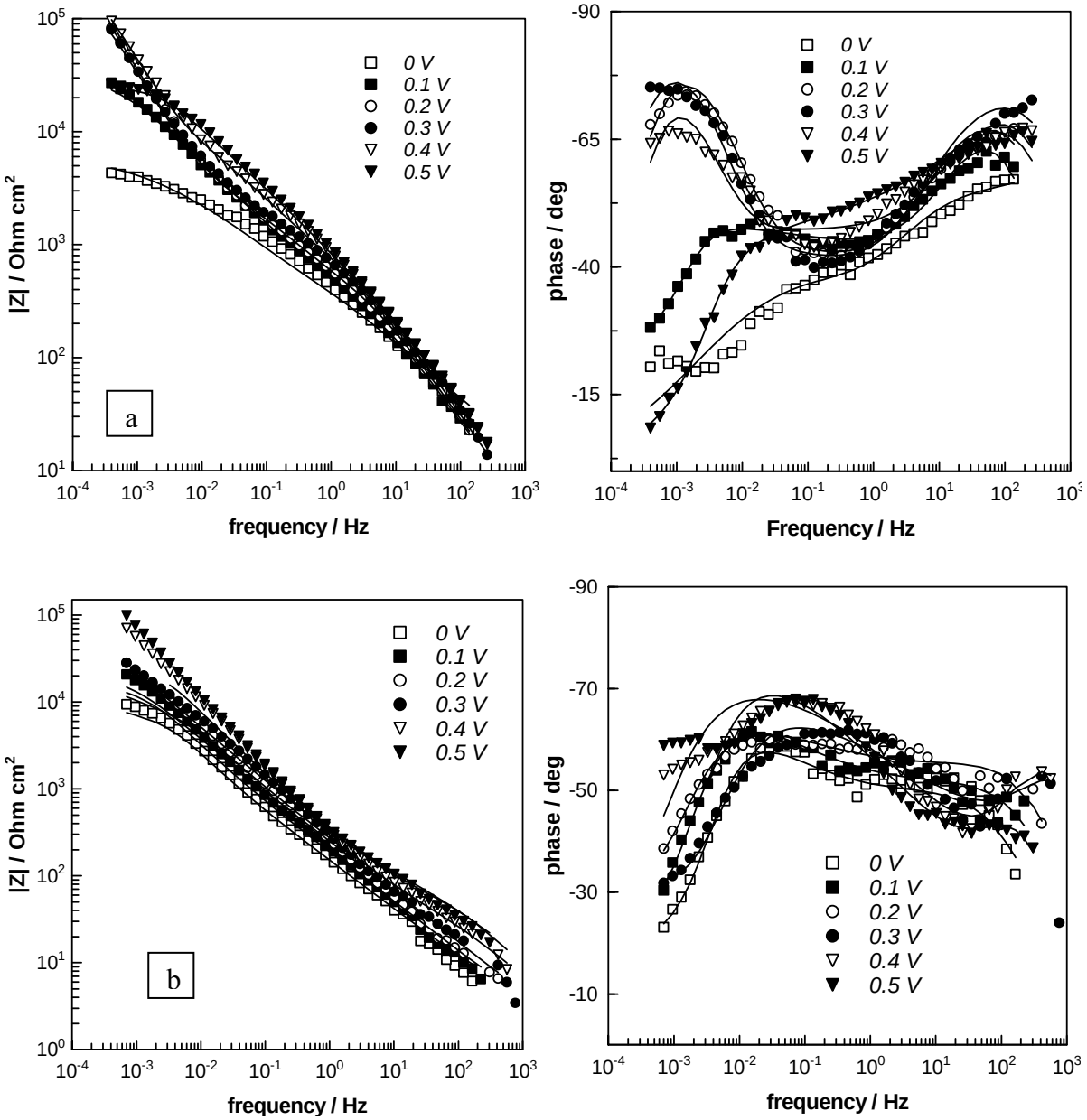

Figure 2. Impedance spectra of AISI 316L(NG) at a range of potentials vs. RHE in simulated PWR water at 280 °C: (a) without Zn, (b) with 1 ppm Zn. Oxidation time 48 h. Left column – impedance magnitude vs. frequency, right column – phase angle vs. frequency. Points – experimental values, solid lines – best-fit calculation according to the model outlined in the text.

The obtained spectra are broadly analogous to those published earlier for austenitic stainless steels and nickel-based alloys [4, 5]. The impedance magnitude at low frequency, $|Z|_{f\to 0}$, that can be assumed to be inversely proportional to the steady-state conductivity of the alloy/oxide/electrolyte system, in general increases with potential in the passive region (from 0 to ca. 0.3-0.4 V), decreasing for higher potentials probably due to the onset of transpassivity and/or oxygen evolution. For the films formed in the simulated PWR water with 1 ppm Zn, the values of $|Z|_{f\to 0}$ are somewhat higher at low potentials in the passive range. This indicates a lower steady-state conductivity of the system, i.e. lower rates of the processes of film growth and restructuring in the presence of Zn (Figure 2a-b). The parameter $|Z|_{f\to 0}$ exhibits in general lower values in the $Na_2B_4O_7$-containing electrolyte when compared to the plain simulated PWR water (Figure 2a and Figure 3a). This observation could be explained by the different composition of the oxide formed in an electrolyte with higher pH (~9 vs. 6.4, see also below). However, in the potential range 0.1-0.4 V, the values of $|Z|_{f\to 0}$ for the films that were subjected to Zn injection are

ca. two times larger than for films grown in the absence of Zn also in the $Na_2B_4O_7$-containing electrolyte. This observation points to a decelerating effect of Zn on the rates of the processes close to steady-state also in this case (Figure 3a-b). Conversely, the value of $|Z|_{f\rightarrow 0}$ at 0.5 V is significantly lower in the Zn-containing solution, which may point to the fact that transpassivity starts earlier in the presence of Zn.

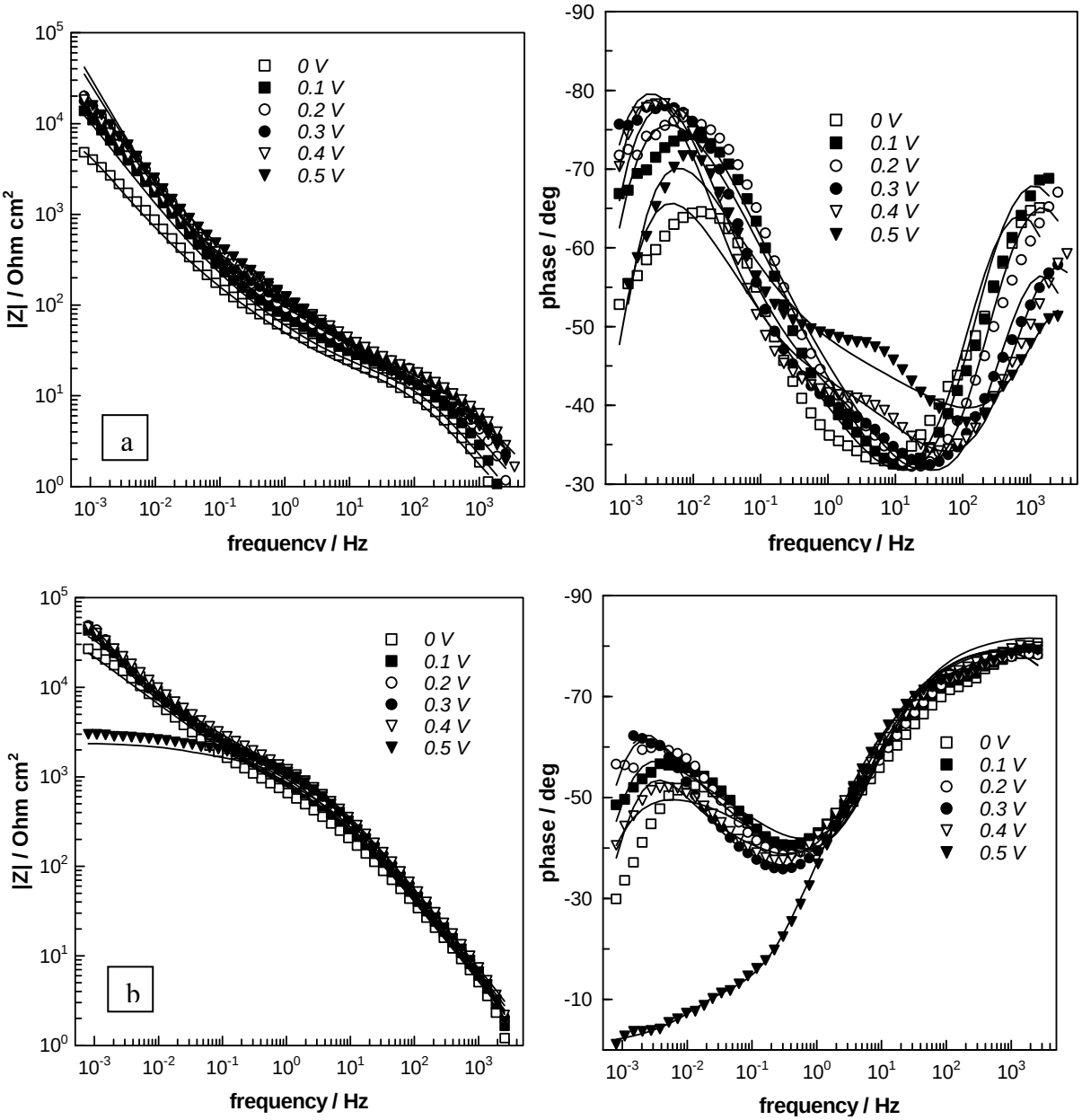

Figure 3. Impedance spectra of AISI 316L(NG) at a range of potentials vs. RHE in simulated PWR water+0.01 M $Na_2B_4O_7$ at 280 °C: (a) without Zn, (b) with 1 ppm Zn. Oxidation time 48 h. Left column – impedance magnitude vs. frequency, right column – phase angle vs. frequency. Points – experimental values, solid lines – best-fit calculation according to the model outlined in the text.

A total of three time constants could be detected in the phase angle vs. frequency curves by preliminary deconvolution of the impedance spectra. Following previous interpretations of impedance spectra in high-temperature electrolytes [5], the highest frequency time constant is associated with the electronic properties of the inner, continuous layer of the oxide film, the medium frequency time constant most probably reflects the ion and electron transfer processes at the oxide/electrolyte interface and the lowest-frequency time constant is assigned to the transport

of point defects in the inner layer of oxide. No contribution of the outer layer was discerned in the spectra most probably due to the fact that it represents a conductive oxide phase consisting of discrete crystallites, as commented also in previous work [1,4]. In what concerns the effect of Zn, it can be stated that Zn injection leads to significant alterations in the phase angle vs. frequency curves in both electrolytes, affecting the frequency ranges of all the three time constants in the spectra. This effect of Zn seems to be more pronounced in the case of the plain simulated PWR water, which could be due to the fact that a significant pH decrease (down to pH 3, measured at room temperature after autoclave cooldown) occurred during the measurements, most probably leading to a more profound alteration in the composition and properties of the oxide layers formed on the stainless steel. Proofs for that statement are sought in the ex-situ characterisation of the in-depth composition of the oxides that are described below. However, it is worth noting that the effect of Zn on the phase angle vs. frequency curves is significant also in the tetraborate-containing electrolyte, in which no pH excursion has been observed (the pH at the beginning and at the end of the experiments was close to 9). This allows the conclusion that the effect of Zn on the electrical and electrochemical properties of the oxides on AISI 316L(NG) in PWR water is not only due to the pH excursion provoked by the hydrolysis reactions of Zn, as commented also by others [6].

6.1.2 Estimation of the in-depth composition of the oxide films with XPS

The XPS depth profiles of the oxides formed on AISI 316L(NG) in simulated PWR water without Zn for 96 h at open circuit (close to 0 V vs. RHE) and during potentiostatic polarisation at 0.5 V RHE are shown in Figure 4, and the corresponding profiles for the oxides formed for 24 h in the absence of Zn followed by Zn injection and 72 h oxidation in a Zn-containing electrolyte are presented in Figure 5. The left columns of the figures represent the in-depth values of the concentrations of the elements considered in the XPS analysis. In these figures, the total concentration of Cr (Cr,%) is calculated as the sum of the concentration of Cr(III) bound as chromium oxide, (Cr(III),%) and the concentration of chromium metal (Cr(0),%) [7]. The right columns in Figure 4- Figure 5 show a comparison between the in-depth variations of the contents of metallic constituents normalised to the total metallic content in order to exclude the effect of oxygen on the depth profiles [1,4,7,]. The oxide thickness was estimated by determining the inflection point of the oxygen depth profiles at which the oxygen concentration falls to 50% of its maximum value via sigmoidal fitting. The position of the alloy/oxide interface is indicated in the right columns of the figures with a vertical line. The boundary between the inner and outer layers has been estimated by sigmoidal fitting of the Fe profiles in analogy to results reported earlier [1] and is also shown in the figures.

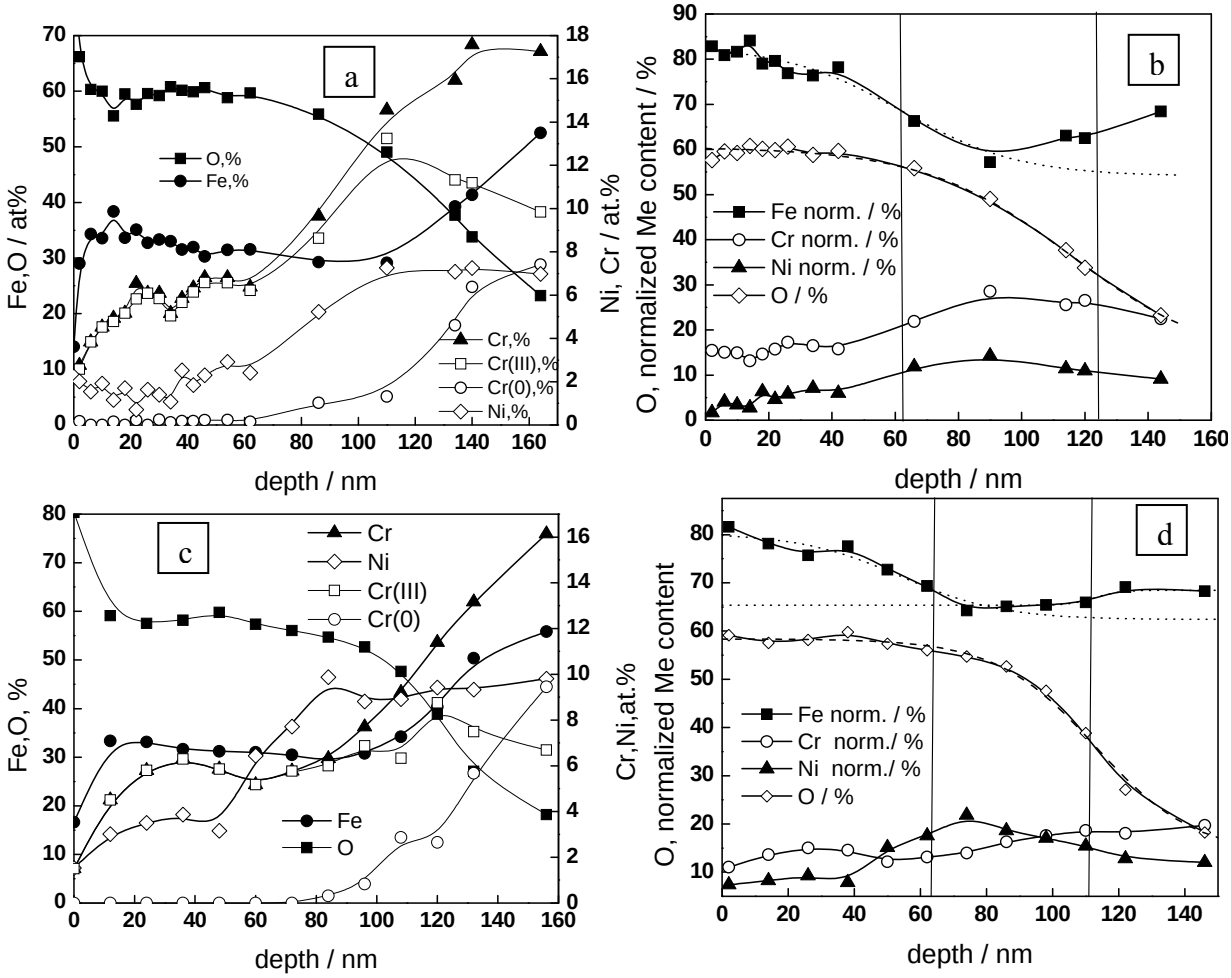

Figure 4. XPS depth profiles of the oxides formed on AISI 316L(NG) in simulated PWR water without the addition of Zn at 280 °C at open circuit (a,b) and at 0.5 V vs. RHE (c,d). (a,c) – atomic concentrations vs. depth, (b,d) – atomic concentration of oxygen and Ni, Cr and Fe contents normalised to the total metallic content of the film.

Both the thicknesses and the in-depth compositions of the oxides formed in Zn-free simulated PWR water are in general agreement with earlier results by a range of authors [8-11]. The effect of potential on thickness and in-depth composition is not very significant, the only noticeable change being the decrease of Cr(III) content in the oxide at the potential of 0.5 V when compared to that at open circuit, and the corresponding increase in Ni content of the oxide (Figure 4). These effects can be explained by the loss of Cr(III) via oxidative dissolution as Cr(VI). On the other hand, the effect of Zn injection on the thickness and composition of the oxides is much more pronounced – the thickness of the oxide decreases ca. 6 times at open circuit and more than 2 times at 0.5 V RHE (cf. Figure 4and Figure 5), the outer layer is practically absent (only a very thin layer containing boron is detected at the potential of 0.5 V) and the Cr content of the inner layer is significantly increased (more than twice, both at o.c. and at 0.5 V). For the film formed at 0.5 V in the presence of Zn, also the Ni content is increased with respect to the oxide formed in the blank solution. Zn is incorporated in the oxide at both potentials in significant amounts (a normalised content of several %), its concentration being somewhat larger in the film formed at open circuit (Figure 5). It can be concluded that the injection of 1 ppm Zn to the simulated PWR water causes a dramatic restructuring of the oxide formed on stainless steel for 24 h in Zn-free solution. Part of this effect could be attributed to the decrease of pH due to the hydrolysis reactions of Zn, as discussed already above (a pH decrease would increase the solubility of the main oxide constituents and most notably that of Fe). Thus

we tried to isolate the effect of Zn incorporation by performing measurements in PWR water buffered with $Na_2B_4O_7$.

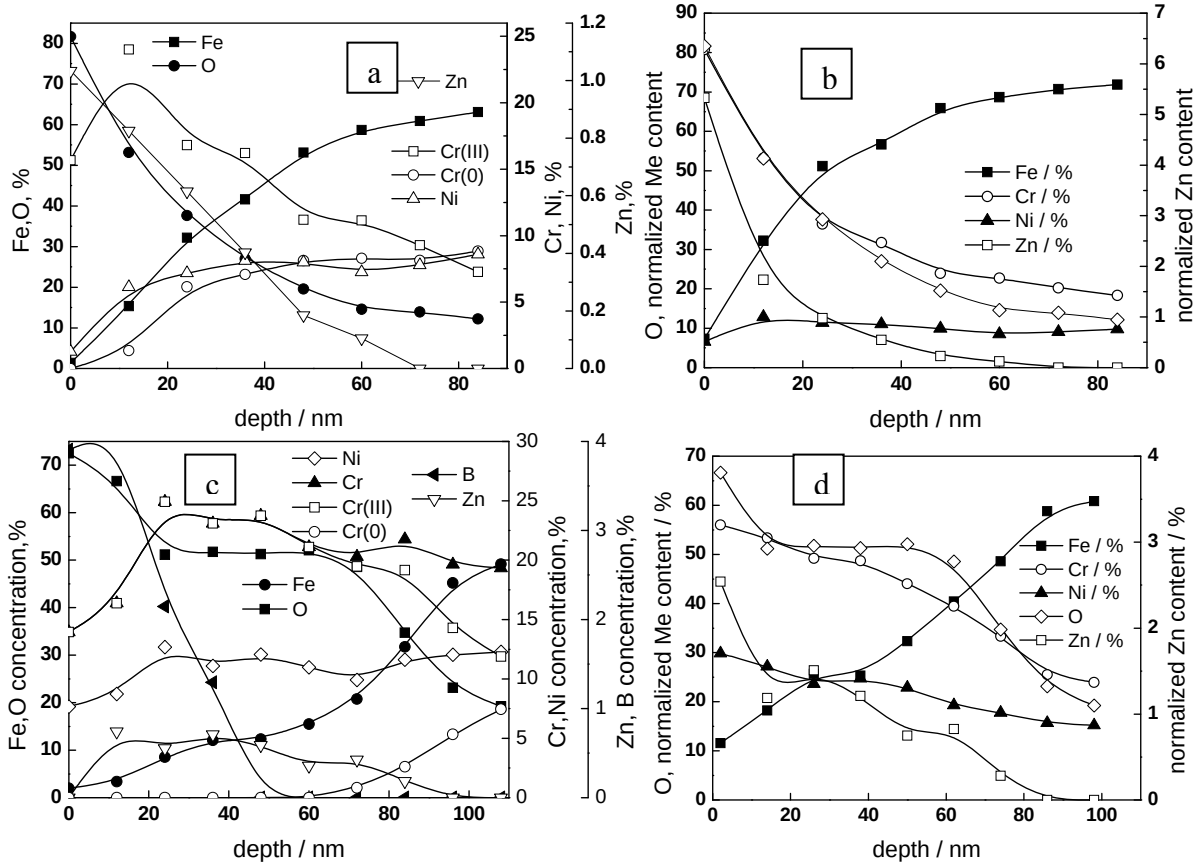

Figure 5. XPS depth profiles of the oxides formed on AISI 316L(NG) in simulated PWR water with 1 ppm Zn at 280 °C at open circuit (a,b) and at 0.5 V vs. RHE (c,d). (a,c) – atomic concentrations vs. depth, (b,d) – atomic concentration of oxygen and Ni, Cr, Zn and Fe contents normalised to the total metallic content of the film.

Figure 6 presents the XPS depth profiles for the films formed in this type of solution at open circuit with and without Zn injection. In the presence of tetraborate, the thicknesses of the films in both Zn-free and Zn-containing electrolytes are more than 2 times larger than those formed in solutions that did not contain tetraborate. This effect could be related to the decrease of the solubility of Fe with increasing pH. Such an explanation is corroborated by the fact that outer layers (i.e. layers that are formed by a dissolution-precipitation mechanism) are observed in both Zn-free and Zn-containing electrolytes and their thicknesses are larger than that of the inner layer. The changes of the in-depth composition of the oxide caused by Zn injection are not as drastic as in the plain PWR water, even if the incorporation of Zn especially in the outer layer is really significant (above 20% of normalised content). This probably means that the outer layer formed by restructuring of the oxide following Zn injection is in fact a mixed Fe-Zn oxide containing small amounts of Ni and Cr. On the other hand, the amount of Zn incorporated in the inner layer stays close of the same order of magnitude as that in the plain PWR water (Figure 5 and Figure 6). A notable effect of Zn injection is that the Ni content of the inner layer formed as a result seems to be larger than that of Cr, which is opposite to the inner layer formed in the absence of Zn. Thus Zn incorporation seems to play an important role in the restructuring of the inner layer also in tetraborate-containing PWR water.

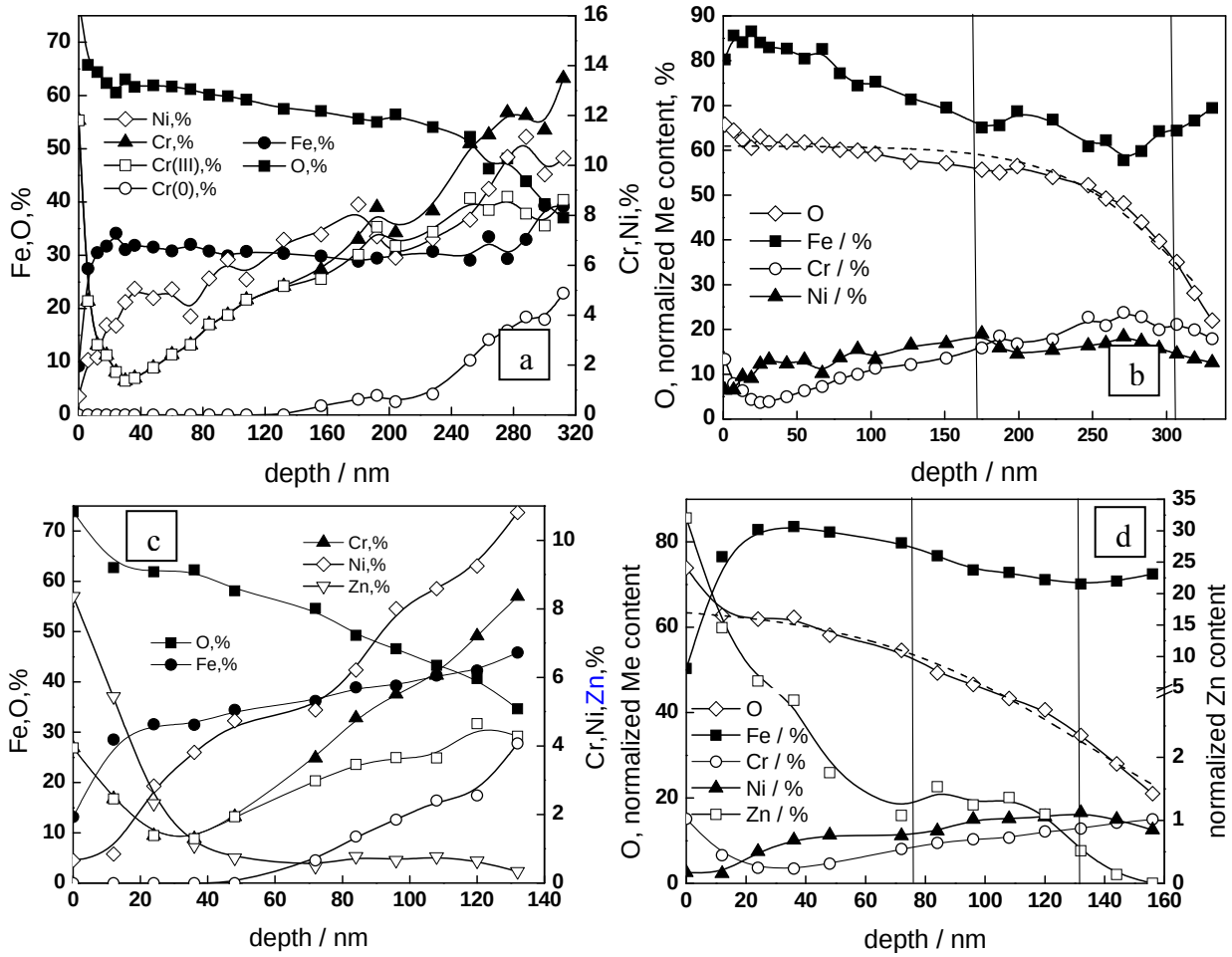

Figure 6. XPS depth profiles of the oxides formed on AISI 316L(NG) in simulated PWR water +0.01 M $Na_2B_4O_7$ without (a,b) and with 1 ppm Zn (c,d) at 280 °C at open circuit. (a,c) – atomic concentrations vs. depth, (b,d) – atomic concentration of oxygen and Ni, Cr, Zn and Fe contents normalised to the total metallic content of the film.

Summarising, Zn injection has a significant effect on the growth and restructuring of the oxides formed for 24 h in both unbuffered and buffered PWR water, altering both the thickness and the in-depth composition of the oxide and hence its electrical and electrochemical properties as reflected by the impedance spectroscopic results. In the following, an attempt to quantify these effects is made within the frames of the MCM.

6.1.3 Modelling of the impedance results

As outlined in the detailed descriptions of the MCM given earlier [1,4,5], the inner layer growth on stainless steel in a high-temperature water electrolyte proceeds via a sequence of reactions involving the generation of normal cation positions and injection of oxygen vacancies at the alloy/film interface, their transport via a diffusion-migration mechanism and subsequent consumption at the film/electrolyte interface via a reaction with adsorbed water. The dissolution of metal through the film followed by the re-deposition of material to form the outer layer is in turn regarded either as a sequence of generation cation interstitials at the inner interface, their transport and consumption at the outer interface, or generation of cation vacancies by ejection of cations at that interface, followed by their transport and reaction at the inner interface to reform normal cation positions. Regardless of the type of defect which is considered predominant in the oxide, the impedance response of the alloy/inner layer/electrolyte system can be approximated as as sum of the impedances of the inner layer Z_f and its interface with the electrolyte $Z_{F/E}$

$$Z = Z_f + Z_{F/E} = \left(Z_e^{-1} + Z_i^{-1}\right)^{-1} + \frac{1}{R_{F/E}^{-1} + j\omega C_{F/E}} \quad (1)$$

where the impedance of the outer interface has been represented as a parallel combination of a charge transfer resistance $R_{F/E}^{-1} = \alpha F(b_c k_c + b_{redox} k_{redox})$ and an interfacial capacitance $C_{F/E}$. For a detailed definition of symbols used throughout the report, the reader is referred to the Nomenclature section.

On the other hand, following previous treatments [5], the impedance of the inner layer Z_f is taken as a sum of the impedances of its electronic properties Z_e and the impedance of transport of defects through it Z_i connected in parallel. In turn, the following expressions have been derived for these impedance components as depending on the kinetic parameters of the reactions of generation k_g and consumption of point defects k_c, the diffusion coefficients of ionic and electronic defects D_e and D_i, the field strength $\vec{E}$ in the inner layer of steady state thickness $\bar{L}$ and the polarisability of the inner layer/electrolyte interface α:

$$Z_e \approx \frac{p}{j\omega C} \ln \frac{\left(1 + j\omega\rho_d \varepsilon\varepsilon_0 e^{\frac{1}{p}}\right)}{1 + j\omega\rho_d \varepsilon\varepsilon_0}, \quad (2)$$

$$p = \frac{1}{2K\bar{L}}, K = \frac{F\vec{E}}{RT}, \bar{L} = L_{E=0} + \frac{1-\alpha}{\vec{E}} E, \rho_d^{-1} = \frac{F^2 D_e}{RT} \frac{k_c}{k_g}$$

$$Z_{ion} = R_t + \frac{RT}{8F^2 K D_i k_g (1-\alpha)\left[\frac{e^{-2K\bar{L}}}{k_c} - \frac{1}{2KD_i}\right]\left[1 + \sqrt{1 + \frac{j\omega}{K^2 D_i}}\right]} \quad (3)$$

It is worth mentioning that according to the MCM [4,5], only the rate constant of consumption of defects at the inner layer/electrolyte interface exhibits a potential dependence: $k_c = k_c^0 e^{b_c E}$ In full analogy to our previous treatments, the impedance that reflects the electronic properties of the oxide has the form of an Young impedance, C being the space-charge layer capacitance of the semiconductor phase in the inner layer, whereas the impedance of ionic transport can be regarded as a generalised Warburg impedance within a layer of finite thickness [4,5].

6.1.4 A model for the in-depth contents of individual metallic constituents

Within the frames of the MCM, the depth profile of a metallic constituent j = Fe, Cr, Ni, or Zn, can be expressed as the dependence of its molar fraction, $y_j = c_j V_{m,MO}$, on the distance within the inner layer, where c_j is its molar concentration and $V_{m,MO}$ the molar volume of the phase in that layer. In order to calculate the depth profiles the respective transient diffusion-migration equations for each component have to be solved [1]

$$\begin{aligned}
\frac{\partial y_{Fe}}{\partial t} &= D_{Fe}\frac{\partial^2 y_{Fe}}{\partial x^2} + \frac{XF\vec{E}D_{Fe}}{RT}\frac{\partial y_{Fe}}{\partial x} \\
\frac{\partial y_{Cr}}{\partial t} &= D_{Cr}\frac{\partial^2 y_{Cr}}{\partial x^2} + \frac{3F\vec{E}D_{Cr}}{RT}\frac{\partial y_{Cr}}{\partial x} \\
\frac{\partial y_{Ni}}{\partial t} &= D_{Ni}\frac{\partial^2 y_{Ni}}{\partial x^2} + \frac{2F\vec{E}D_{Ni}}{RT}\frac{\partial y_{Ni}}{\partial x} \\
\frac{\partial y_{Zn}}{\partial t} &= D_{Zn}\frac{\partial^2 y_{Zn}}{\partial x^2} - \frac{2F\vec{E}D_{Zn}}{RT}\frac{\partial y_{Zn}}{\partial x}
\end{aligned} \tag{4}$$

The negative sign of the migration term in the fourth equation of (4) is due to the fact that Zn is incorporated into the inner layer from the electrolyte interface, i.e. its incorporation proceeds against the field [1]. Such a reaction is considered to be viable for oxides formed on stainless steels in high-temperature water by virtue of the rather low values of the field strength in such conditions [1,4].

The relevant boundary conditions at the alloy/film and film/electrolyte interfaces, as well as the initial conditions are given as

$$\begin{aligned}
&y_{Fe}(x,0) = y_{Fe,a}, y_{Cr}(x,0) = y_{Cr,a}, y_{Ni}(x,0) = y_{Ni,a}, y_{Zn}(x,0) = 0 \\
&y_{Fe}(0,t) = y_{Fe,a}, y_{Cr}(0,t) = y_{Cr,a}, y_{Ni}(0,t) = y_{Ni,a}, y_{Zn}(0,t) = K_{enr}c_{Zn,aq}V_{m,MO} \\
&y_{Fe}(L,t) = \frac{k_{g,Fe}}{V_{m,MO}}\left[\frac{1}{k_{c,Fe}} + \frac{RT}{XF\vec{E}D_{Fe}}\right] \\
&y_{Ni}(L,t) = \frac{k_{g,Ni}}{V_{m,MO}}\left[\frac{1}{k_{c,Ni}} + \frac{RT}{2F\vec{E}D_{Ni}}\right] \\
&y_{Cr}(L,t) = \frac{k_{g,Cr}}{V_{m,MO}}\left[\frac{1}{k_{c,Cr}} + \frac{RT}{3F\vec{E}D_{Cr}}\right] \\
&y_{Zn}(L,t) = K_{enr}c_{Zn,aq}V_{m,MO}
\end{aligned} \tag{5}$$

The boundary conditions for Cr, Fe and Ni at the film/electrolyte interface are given by the steady-state concentrations of the respective metallic constituents at that interface obtained by the steady-state solution of the transport equations [1]. The boundary condition for Zn at the inner layer/outer layer interface is given by the enrichment factor of Zn defined as the ratio between the concentration of Zn at that interface and the Zn concentration in the water, assumed to be independent on the time of exposure.

In the absence of representative information on the pore diameter and tortuousity, and also of reliable data on the crystallite size of the outer layer, the growth of this layer is formally treated as a diffusion process in a matrix constituted of outer layer crystals with electrolyte in between [1]. Such a treatment for the oxide layer has already been presented in relation to incorporation of foreign species into the growing film. Since the outer layer is not continuous but rather represents a system of discrete crystallites with electrolyte in the pores, the role of the potential gradient in this layer can be considered negligible with respect to the concentration gradient. Thus, to calculate the depth profile of a certain cation in the outer layer, the following system of equations has to be solved

$$\begin{aligned}
\frac{\partial y_{Fe,OL}}{\partial t} &= D_{Fe,OL}\frac{\partial^2 y_{Fe,OL}}{\partial x^2} \\
\frac{\partial y_{Cr,OL}}{\partial t} &= D_{Cr,OL}\frac{\partial^2 y_{Cr,OL}}{\partial x^2} \\
\frac{\partial y_{Ni,OL}}{\partial t} &= D_{Ni,OL}\frac{\partial^2 y_{Ni,OL}}{\partial x^2} \\
\frac{\partial y_{Zn,OL}}{\partial t} &= D_{Zn,OL}\frac{\partial^2 y_{Zn,OL}}{\partial x^2}
\end{aligned} \qquad (6)$$

The boundary conditions at the inner interface of the outer oxide layer are identical to those used as outer boundary conditions at the inner layer / electrolyte interface, which ensures the continuity of the composition of the whole film. At this point, the boundary conditions at the outer layer / electrolyte interface are assumed to be equal to the experimentally found stoichiometry of the outermost layer of oxide as estimated by XPS. However, the sorption test results presented later in this report will be used as more exact estimates for the boundary conditions. This refinement of the model is underway.

6.1.5 Calculational procedure

As a first step, impedance spectra for AISI 316L(NG) in the studied electrolytes were fitted to equations (1)-(3) and the values of the parameters $C, k_g, k_c, D_e, D_i, \vec{E}, R_{F/E}$ and $C_{F/E}$ have been estimated in the whole potential range, assuming a dielectric constant ε=25 for the inner layer and a value of the polarisability of the inner layer/electrolyte interface α=0.9 as found from previous calculations based on impedance data for AISI 316L(NG) in borate electrolyte at 250-300°C [**Error! Reference source not found.**]. The results of this fitting are shown in Figure 2 and Figure 3 with solid lines and demonstrate the ability of the model approach to reproduce both the magnitude and the frequency distribution of the impedance in the whole studied range of potentials.

Table 1 Parameter values estimated from the fit of the experimental impedance data to equations (1)-(3) of the MCM. Dielectric constant of the inner layer ε=25 and polarisability of the inner layer/electrolyte interface α=0.9.

Parameter	PWR, 1 ppm Zn		PWR+borate	
	no Zn	1 ppm Zn	no Zn	1 ppm Zn
10^{12} k_g / cm^4 mol^{-1}s^{-1}	7.6	7.9	7.1	6.5
$10^{13}k_c^0$ / cm s^{-1}	4.8	2.2	4.8	4.5
b_c / V^{-1}	1.9	4.0	2.0	2.9
$\vec{E}$, kV cm^{-1}	52	60	57	57
10^{18} D_i / cm^2 s^{-1}	3.0	0.61	4.5	3.8
10^{12} D_e / cm^2 s^{-1}	5.1	3.5	2.6	2.3
$C_{F/E}$ / mF cm^{-2}	4.0	2.6	22.0	3.8

As an illustration of the evolution of the calculated parameters with potential, the dependences of the space charge layer capacitance C, the parameter $\rho_d\varepsilon$ (see Eqn. (2)) and the charge transfer resistance at the inner layer/electrolyte interface $R_{F/E}$ are plotted vs. potential in Figure 7. A summary of the remaining fitting parameter values is given in Table 1. The space charge layer capacitance decreases with potential and the resulting C^{-2} vs. E dependences are linear (Figure 7a), suggesting that the presence of an n-type semiconductor phase in the inner layer. Notwithstanding all the limitations of the use of a simple Mott-Schottky approach to that layer, it

is worth mentioning that the apparent donor densities calculated from the slope of the C^{-2} vs. E dependences in general decrease in the presence of Zn. This seems to be in accordance to the presumed decrease of the concentration of ionic defects playing the role of electron donors for the films restructured after the injection of Zn to the electrolyte. The $\rho_d\varepsilon$ dependence (Figure 6b) is to a certain extent analogous to that obtained earlier for AISI 316L(NG) in 0.1 M $Na_2B_4O_7$ in the temperature interval 250-300°C [4] and also demonstrates the presence of an n-type semiconductor layer in the most part of the passive region. The values of this parameter are the largest for the film formed and restructured in plain simulated PWR water with Zn injection, which could be correlated to the highest Cr content of this film as evidenced by XPS (Figure 5). The dependences of the charge transfer resistance at the film/electrolyte interface $R_{F/E}$ on potential (Figure 7c) suggest that a redox reaction dominates over the ionic transfer reactions at this interface. The exponential coefficients of the cathodic branch of the curves approximating this dependence (ca. 6 V^{-1}, Figure 7c) are larger than those for the anodic branch (ca. 2 V^{-1}) which is consistent with a charge transfer reaction on an n-type semiconductor layer.

Next, estimates for the rate constants and diffusion coefficients of individual metallic constituents of the inner layer, as well as the apparent diffusion coefficients during outer layer growth were estimated. This was done by a quantitative comparison of the XPS depth profile data with the solutions of equations (5) and (6) to obtain the best match between experimental and calculated values, introducing the following restrictions for the parameters stemming from the above calculations based on impedance data:

$$\begin{aligned} k_g &= k_{g,Fe}y_{Fe,a} + k_{g,Cr}y_{Cr,a} + k_{g,Ni}y_{Ni,a} \\ k_c &= k_{c,Fe}y_{Fe}(L,t) + k_{c,Cr}y_{Cr}(L,t) + k_{c,Ni}y_{Ni}(L,t) \\ D_i &= D_{Fe}y_{Fe,a} + D_{Cr}y_{Cr,a} + D_{Ni}y_{Ni,a} + D_{Zn}y_{Zn}(L,t) \end{aligned} \qquad (7)$$

For the purpose, the contents of the each metallic constituent of the oxide were normalised to the total metallic content to calculate the respective mass fractions and the depth was recalculated as distance from the alloy/oxide interface using the estimates of inner and outer layer thicknesses obtained as discussed above. An example of the plots of the mass fractions vs. the distance from the alloy/oxide interface is presented in Figure 8 (for AISI 316L(NG) in the plain simulated PWR water). The calculated curves (solid lines) are in good agreement with the experimental data (points), indicating that the model is once again able to account for the essential features of the data. Sensitivity analyses performed in our previous paper [1] by estimating the effect of a 10% change of the respective kinetic parameters on the calculated depth profiles have demonstrated that the obtained values are significant and can be used to explore further the transport mechanism through the oxide. The values of the kinetic and transport parameters estimated on the basis of the above procedure are listed in Table 2. A more detailed description of the calculation results and the analyses of the obtained parameters will be given in a subsequent scientific paper written on the results presented in this report.

Table 2 Kinetic parameters of film growth and restructuring on AISI 316L(NG) at 280 °C in PWR water as estimated by the proposed procedure.

Parameter	PWR, no Zn		PWR, 1 ppm Zn		PWR+borate,o.c.	
	o.c.	0.5 V RHE	o.c.	0.5 V RHE	no Zn	1 ppm Zn
$10^{12}\, k_{g,Cr}$ / cm^4 mol^{-1}s^{-1}	8.0	8.0	9.0	6.0	9.0	7.0
$10^{12} k_{g,Fe}$ / cm^4 mol^{-1}s^{-1}	8.0	8.0	8.0	7.0	7.0	7.0
$10^{12} k_{g,Ni}$ / cm^4 mol^{-1}s^{-1}	4.0	5.0	2.5	4.0	4.0	4.0
$10^{13} k_{c,Cr}$ / cm s^{-1}	7.0	15.0	3.0	3.0	15	20
$10^{13} k_{c,Fe}$ / cm s^{-1}	3.2	3.0	20.0	15	2.3	2.0
$10^{13} k_{c,Ni}$ / cm s^{-1}	7.0	6.0	5.0	3.0	6.0	7.0
$\vec{E}$, kV cm^{-1}	57	52	80	40	57	57
$10^{18}\, D_{Cr}$ / cm^2 s^{-1}	3.7	3.0	0.5	4.0	3.7	2.7
$10^{18}\, D_{Fe}$ / cm^2 s^{-1}	2.5	2.2	0.7	5.0	5.0	4.0
$10^{18}\, D_{Ni}$ / cm^2 s^{-1}	3.5	3.0	0.4	5.0	3.5	2.5
$10^{18}\, D_{Zn}$ / cm^2 s^{-1}	-	-	0.5	3.0	-	5.5
$10^{16}\, D_{Cr,OL}$ / cm^2 s^{-1}	5.0	5.0	-	-	5.0	0.030
$10^{16}\, D_{Fe,OL}$/ cm^2 s^{-1}	6.0	6.0	-	-	6.0	0.055
$10^{16}\, D_{Ni,OL}$/ cm^2 s^{-1}	7.0	7.0	-	-	7.0	0.030
$10^{16}\, D_{Zn,OL}$/ cm^2 s^{-1}	-	-	-	-	-	0.10

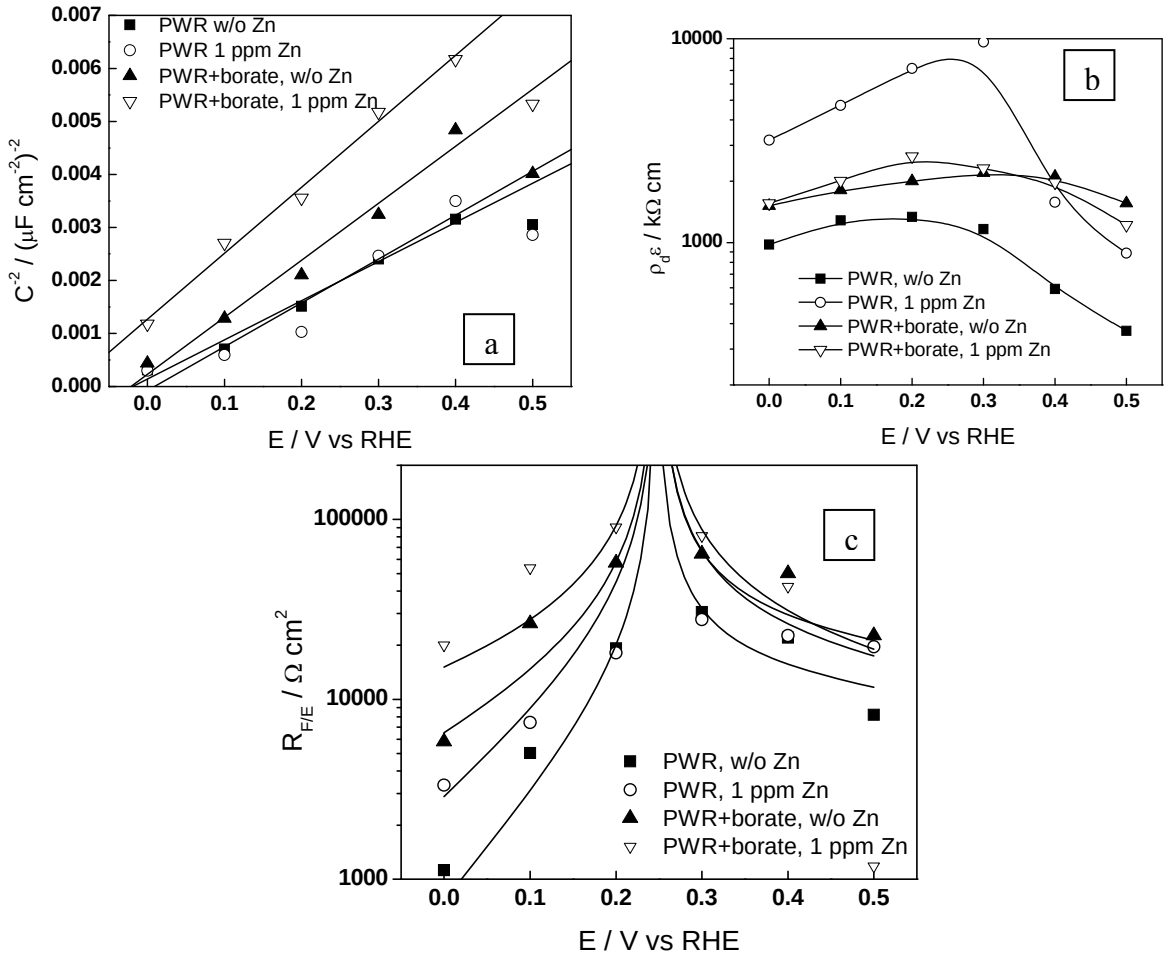

Figure 7. Dependences of the space charge capacitance of the inner layer (a), the parameter $\rho_d \varepsilon$ (b) and the charge transfer resistance at the film/electrolyte interface (c) on potential

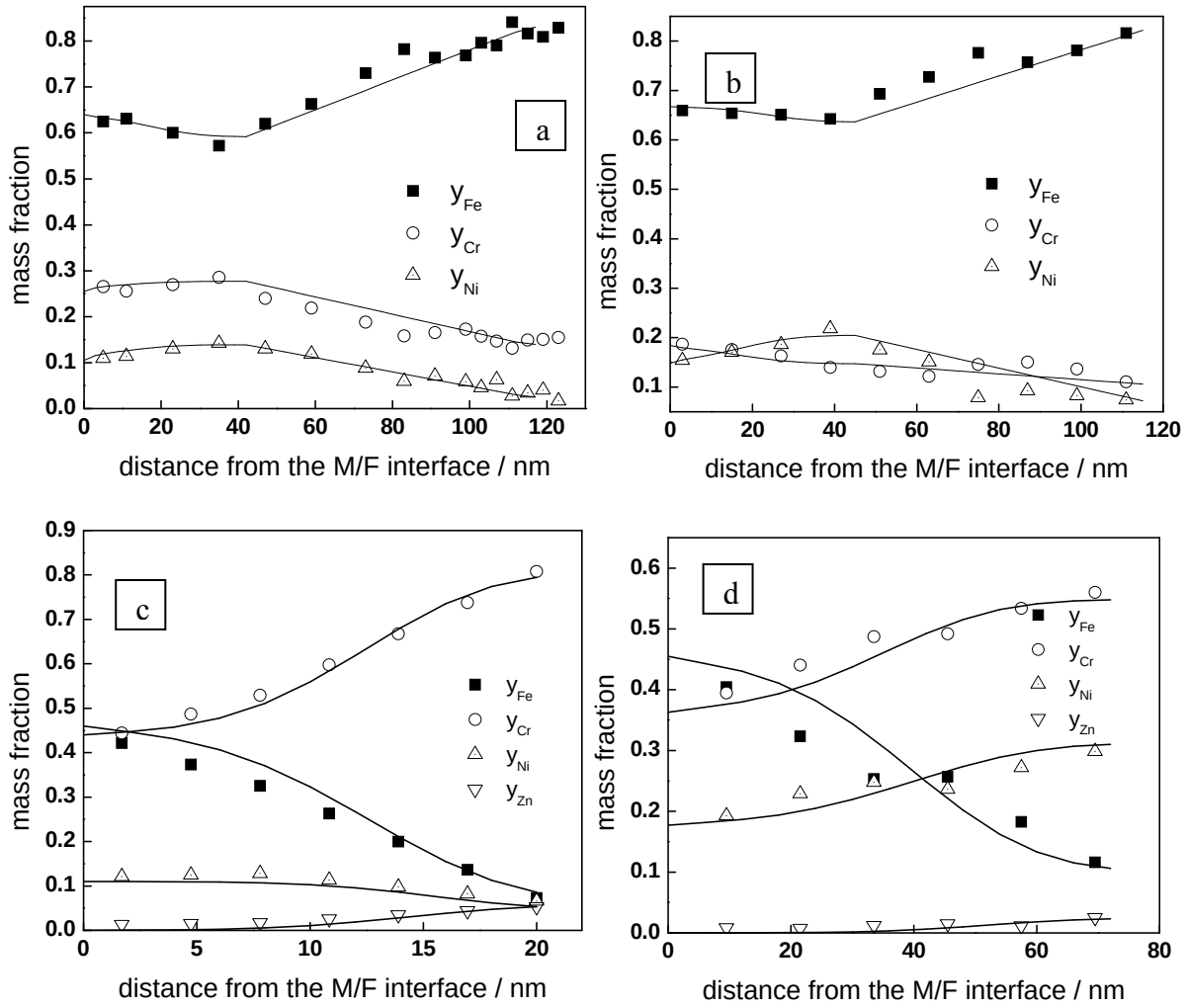

Figure 8. Experimental (points) and calculated (solid lines) mass fractions of the main metallic constituents of the oxides formed on AISI 316L(NG) in simulated PWR water (1200 ppm B, 2 ppm Li) at 280 °C at open circuit (a,c) and at 0.5 V vs. RHE (b,d) without Zn (a,c) and with 1 ppm Zn (b,d).

6.2 Sorption test results

6.2.1 Determination of surface site concentration on magnetite

In order to adjust the wanted surface coverage for the sorption tests, the number of surface sites, i.e. proton/cation binding sites, on the oxide had to be determined. As mentioned above in Chapter 5.2, the surface site concentration for magnetite was determined in this work as the corresponding value for hematite had been determined already in an earlier project (7.5×10^{-7} mol g^{-1} or 0.9×10^{-7} mol m^{-2} [2]). The surface site concentration was determined both at ambient temperature and at 280°C. The titration results obtained at ambient temperature are given in Figure 9.

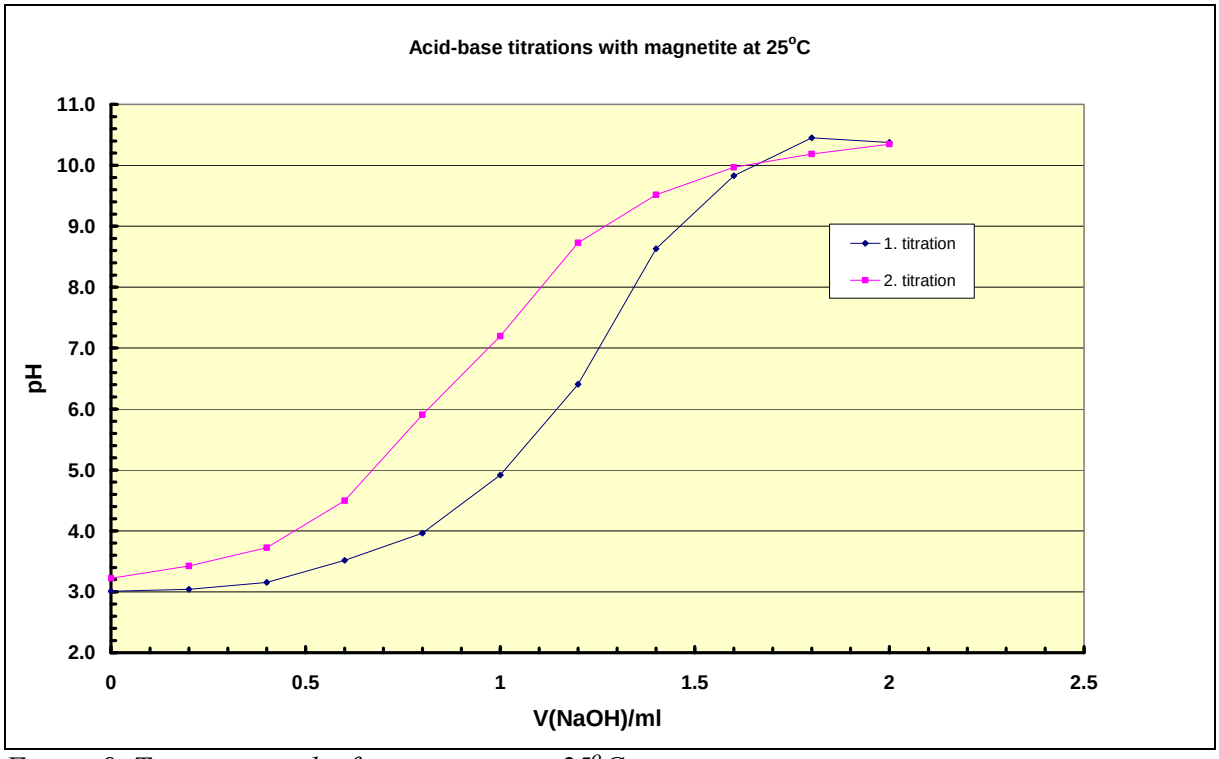

Figure 9. Titration results for magnetite at 25°C.

The analysis procedure of Gran [3] potentiates an accurate determination of excess protons, H_o, which is used to calculate the amount of adsorbed protons, H_s, as the difference

$$H_s = H_{added} - H_o \qquad (8)$$

The free proton concentration during the first part of the titration can be expressed as

$$[H^+] = (H_o - V_t c_t) / (V_t + V_{beg}) \qquad (9)$$

where V_{beg} is the volume of the titrated suspension in the beginning of the titration
V_t is the added volume of the titrant
H_o is the amount of excess protons in the beginning of the titration
c_t is the concentration of the titrant (NaOH)

Combining this equation with the expression for the electromotive force of the measurement cell

$$E_H = E_{o,H} + 59.157 \text{ mV } \log[H^+] + E_j \qquad (10)$$

where $E_{o,H}$ is the apparatus constant
E_j is the liquid junction potential depending on ionic strength and free hydrogen ion concentration,

gives

$$E_H = E_{o,H} + E_j + (0.059157\ \mathrm{V})\log\left(\frac{H_o - V_t c_t}{V_{beg} + V_t}\right) \quad (11)$$

which can be further written in the form

$$10^{\frac{E_H}{0.059157\mathrm{V}}} = 10^{\frac{E_{oH}+E_j}{0.059157\mathrm{V}}}\left(\frac{H_o - V_t c_t}{V_{beg} + V_t}\right) \quad (12)$$

$$(V_{beg} + V_t)10^{\frac{E_H}{0.059157\mathrm{V}}} = 10^{\frac{E_{oH}+E_j}{0.059157\mathrm{V}}}(V_{ef} - V_t)c_t \quad (13)$$

where V_{ef} is the equivalent volume of the titrant defined as $H_o = V_{ef}c_t$.

When the left-hand side of equation (13) (the Gran function) is plotted as a function of V_t, a straight line intercepting the V_t axis at V_{ef} is obtained. Actually, the linearity of the plot indicates that there is an excess of free hydrogen ions in this pH region. Further, the glass electrode can be calibrated *in situ* on a concentration scale employing the data observed in this acidic region. The sum, $E_{o,H} + E_j$, can be obtained from the slope of the Gran plot.

In this work the Gran analysis was used both at ambient and elevated temperatures. For the measurements at ambient temperature, as a commercial glass electrode was used, the emf of the measurement system is not known exactly and cannot be split into separate potential terms as written in Eq. (13), but a pseudo-"Gran" plot has been drawn by grouping all the potential terms in Eq. (11) as

$$\mathrm{pH} = -\log[H^+] = -(E_H - E_{o,H} - E_j)/0.059157\ \mathrm{V} \quad (14)$$

Fitting this term into Eq. (13) gives

$$(V_{beg} + V_t)10^{\frac{E_H - E_{oH} - E_j}{0.059157\mathrm{V}}} = (V_{beg} + V_t)10^{-pH} = (V_{ef} - V_t)c_t \quad (15)$$

Instead of the "true" Gran function (left hand side of Eq. (13)), $(V_{beq}+V_t)10^{-pH}$ vs. V_t is plotted in Figure 10. The amount of added HNO_3 in the beginning of the test was 4×10^{-4} mol. From the equations of the fitted trendlines, it can be seen that averaged $V_{ef} \sim 0.84$ ml, which means that 8.4×10^{-5} mol of NaOH (0.1M) is needed to neutralize the excess acid in the solution. Hence, $3.2\cdot10^{-4}$ mol of protons were adsorbed on the surface, implying a surface site density of $3.2\cdot10^{-5}$ mol g^{-1} (10g magnetite used, specific area ~40m^2 g^{-1}) or $7.9\cdot10^{-7}$ mol m^{-2}. This value coincides very well to the values given in literature for the magnetite surface site concentrations: $2\text{-}5\times10^{-5}$ mol g^{-1} [12, 13].

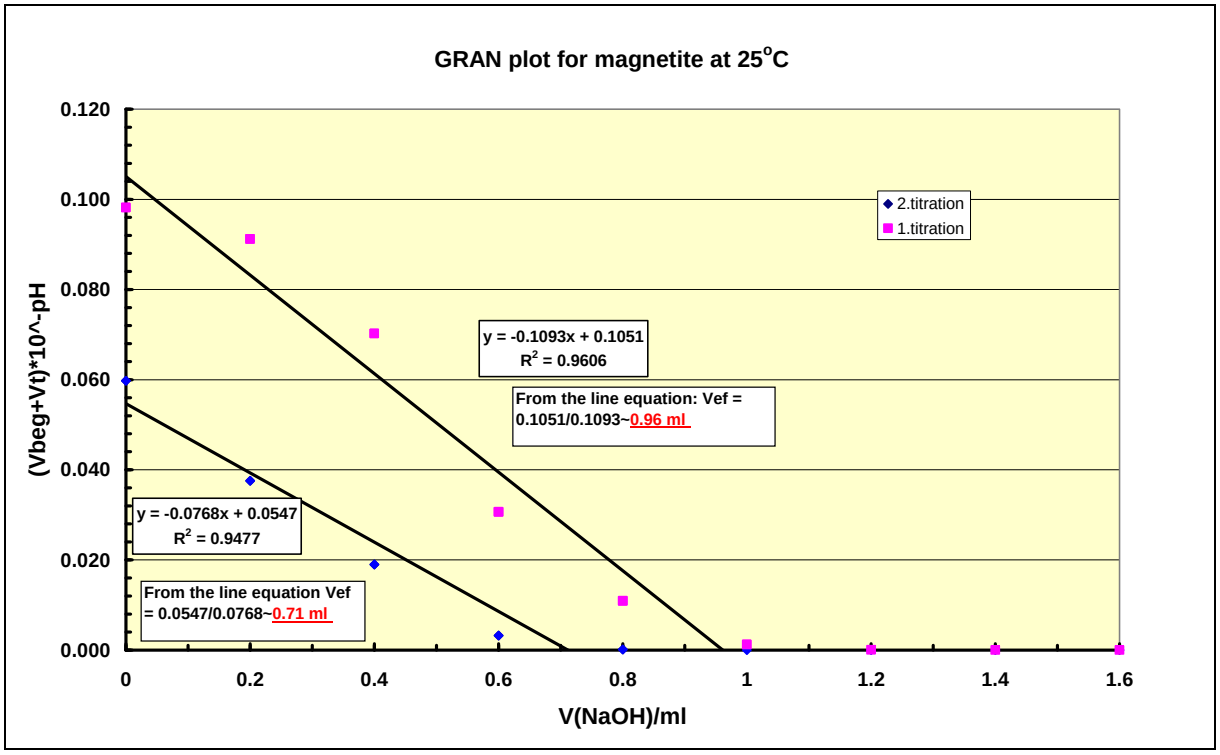

Figure 10. Gran plot analysis to determine the excess acid in solution and, consequently, the amount of adsorbed protons and the density of surface sites for magnetite at 25°C.

The titration results at 280°C are shown in Figure 11. At 280°C the denominator the exponent in Eq (13) is ca. 0.11 V instead of 0.059157 V

$$(V_{\mathrm{beg}} + V_{\mathrm{t}})10^{\frac{E_{\mathrm{H}}}{0.11\mathrm{V}}} = 10^{\frac{E_{\mathrm{oH}} + E_{\mathrm{j}}}{0.11\mathrm{V}}}(V_{\mathrm{ef}} - V_{\mathrm{t}})c_{\mathrm{t}} \qquad (16)$$

The true Gran function is plotted in Figure 12 and from the fitted trendline it can be calculated that in the two measurements V_{ef} ~ 20.46 and 16.45 ml, which means that 2.05×10^{-3} mol and 1.65×10^{-3} mol of NaOH is needed to neutralize the excess acid in the solution. Hence, as the amounts of added acid in the two measurements were 5.37×10^{-3} mol and 5.27×10^{-3} mol, 3.32×10^{-3} mol and 3.63×10^{-3} mol of protons was adsorbed on the surface. This implies an averaged surface site density of 6.95×10^{-5} mol g^{-1} (50g magnetite used) or 17.5×10^{-7} mol m^{-2}. This value is roughly twice the surface site density determined at 25°C.

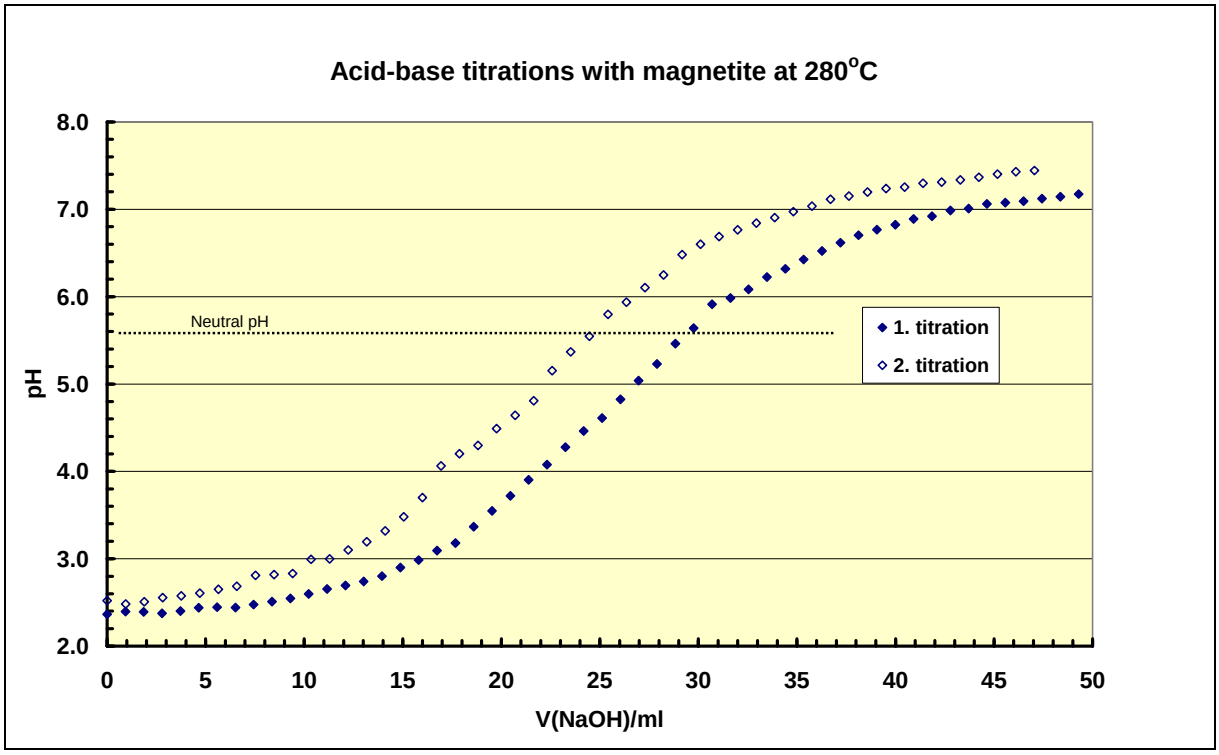

Figure 11. Titration results for magnetite at 280°C.

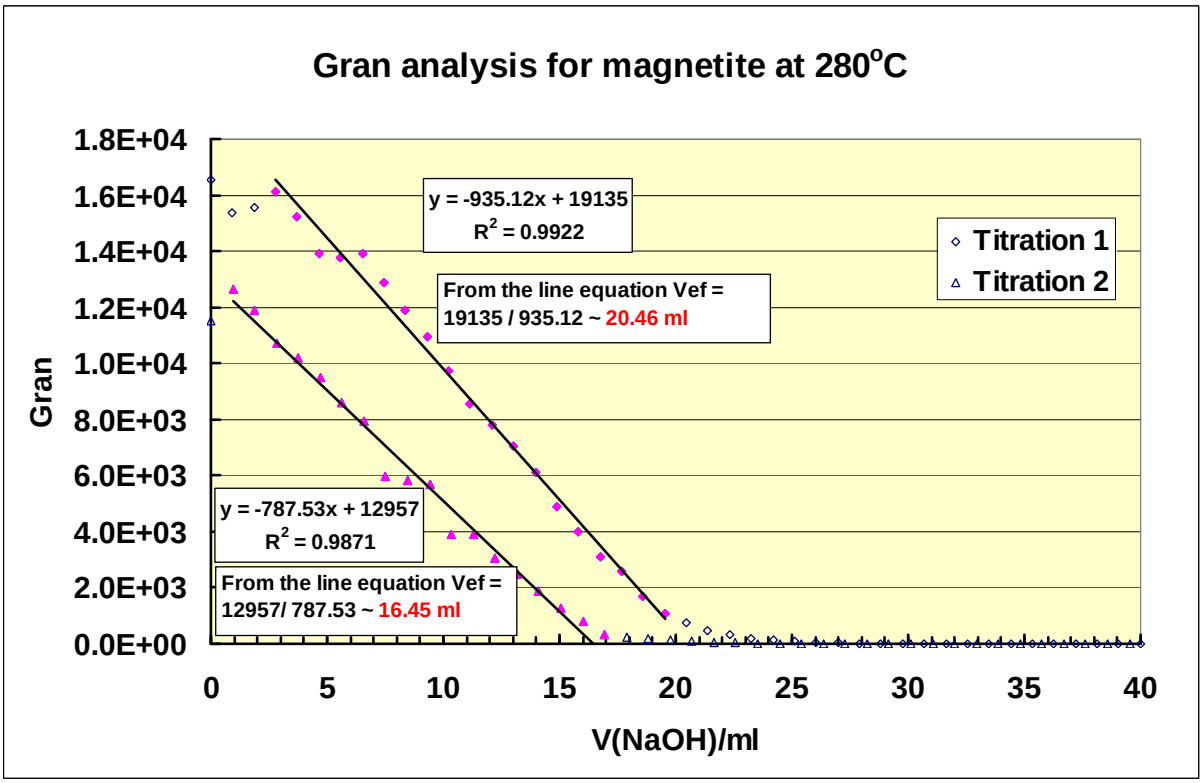

Figure 12. Gran plot analysis to determine the excess acid in solution and, consequently, the amount of adsorbed protons and the density of surface sites for magnetite at 280°C.

6.2.2 Batch test results

A series of batch tests to study sorption of different cations (i.e. Ni, Zn, Co and Sb) was performed on both hematite and magnetite. The solution concentration prior to sorption was selected to be rather high (1 ppm) to simulate normal operating plant conditions, but anyway it

was considered possible in some extreme conditions. Another point to be taken into account in the batch tests was that the solution concentration needed to be set to a low enough level to avoid surface re-precipitation. The results from the tests are shown in Table 3 (hematite) and Table 4 (magnetite) and in . The cation species in the tables present the total amount of all possible complex species existingin the solution. Therefore, no separation between different hydrolysed complexes is not shown but, for example, all the Zn based species are included in the Zn^{2+} amount given in the tables.

Table 3. Sorption test results on hematite at 280°C.

	TEST 1			TEST 2		
Cation	A) Surface coverage if all surface sites would have been occupied after cation addition, %	B) Measured surface coverage,%	Sorption-% (=B/A)	A) Surface coverage if all surface sites would have been occupied after cation addition, %	B) Measured surface coverage,%	Sorption-% (=B/A)
Zn^{2+}	14.67	14.34	97.803389	11.33	10.59	93.45106
Ni^{2+}	13.33	3.76	28.199012	13.47	5.22	38.79572
Co^{2+}	13.27	12.38	93.280504	12.80	12.54	97.94954
Sb^{3+}	6.79	6.73	99.16129	6.59	6.45	97.90698

Table 4. Sorption test results on magnetite at 280°C.

	Cation			
	Zn^{2+}	Ni^{2+}	Co^{2+}	Sb^{3+}
TEST 1				
THEORETICAL SURFACE COVERAGE	*1-3%*			
A) Surface coverage if all surface sites would have been occupied after cation addition, %	2.34	2.81	2.44	1.16
B) Measured surface coverage,%	2.29	2.68	2.38	0.70
Sorption-% (=B/A)	97.72	95.36	97.57	60.81
TEST 2				
A) Surface coverage if all surface sites would have been occupied after cation addition, %	2.36	2.80	2.46	1.28
B) Measured surface coverage,%	2.28	2.67	2.43	0.90
Sorption-% (=B/A)	96.62	95.53	98.80	70.75
TEST 3				
THEORETICAL SURFACE COVERAGE	*10 %*			
A) Surface coverage if all surface sites would have been occupied after cation addition, %			9.60	9.97
B) Measured surface coverage,%			7.74	9.44
Sorption-% (=B/A)			80.66	94.61
TEST 4				
A) Surface coverage if all surface sites would have been occupied after cation addition, %			9.79	9.94
B) Measured surface coverage,%			7.78	9.50
Sorption-% (=B/A)			79.47843	95.61983471

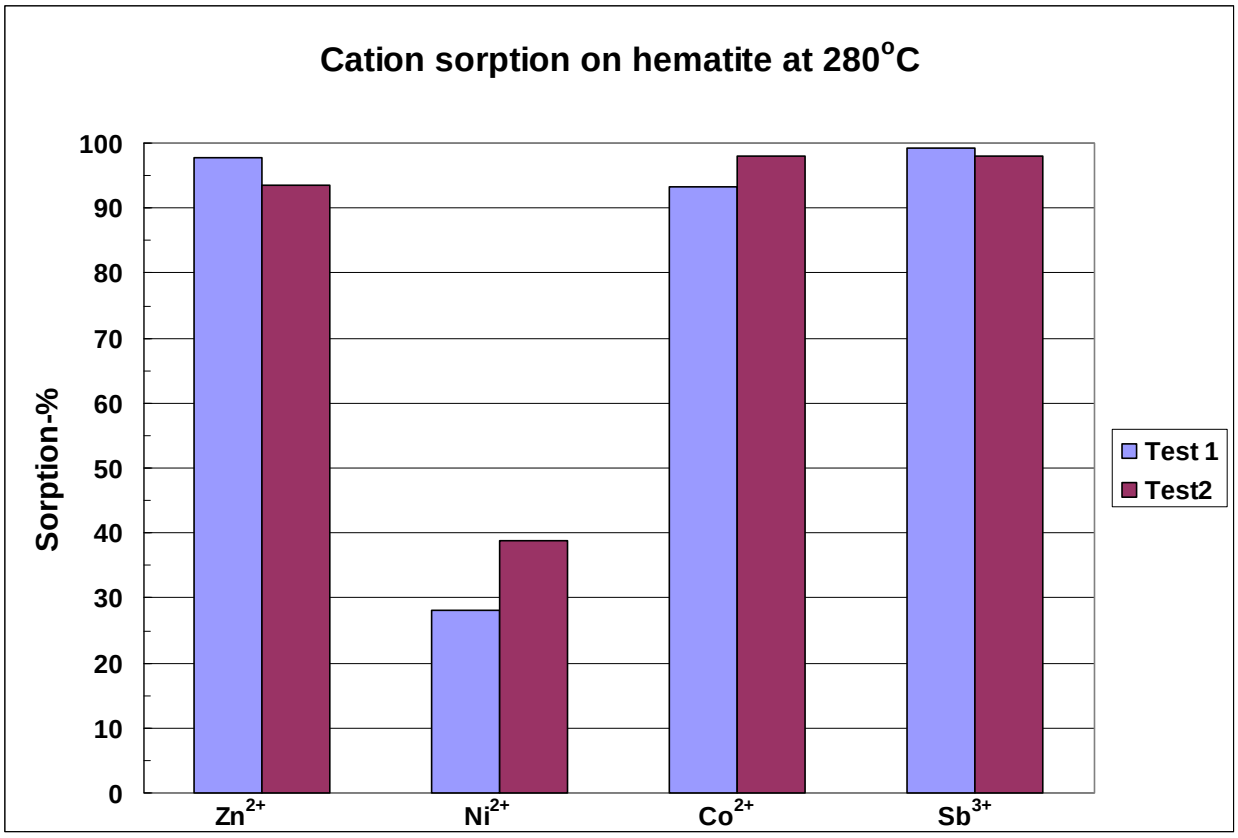

Figure 13. Sorption of cations on hematite at 280°C in simulated PWR coolant.

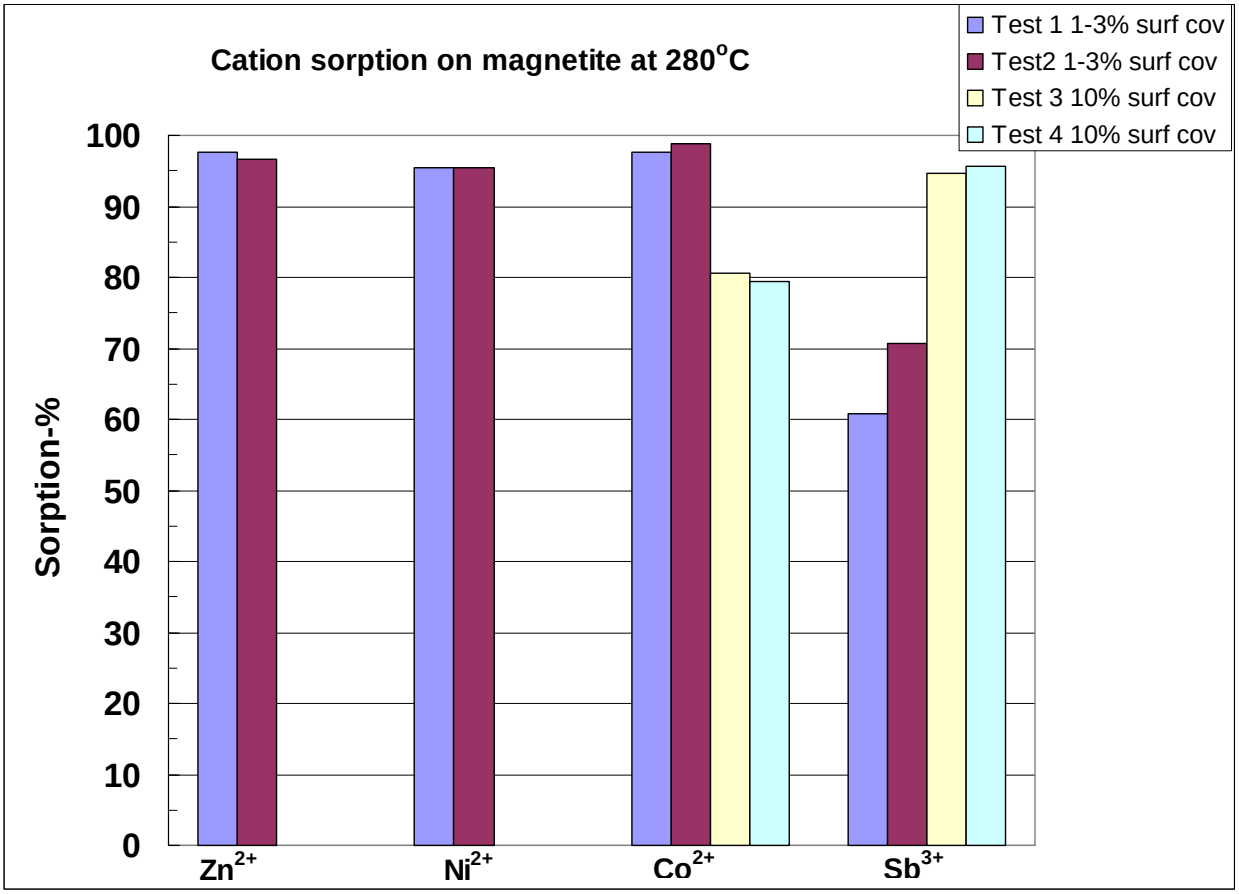

Figure 14. Sorption of cations on magnetite at 280°C in simulated PWR coolant.

The results from Table 3 and Figure 13 indicate that in the case of hematite the sorption of all other cations except Ni^{2+} occurs almost totally with the surface coverages employed. The kinetics of sorption was studied for the Sb solution by taking samples after 5, 10 and 15 minutes. The sorption % increases only slightly in that time being 6.45% after 5 minutes and 6.47% after 15 minutes, indicating that on hematite the sorption reaction is very fast at this specific surface coverage.

The results for magnetite at low surface coverages (1-2%,
Table 4 and Figure 14) indicate that Sb^{3+} attaches to the surface at 60-70% of the theoretical full sorption (tests 1 and 2). For all other cations the sorption is almost total (over 90%). On the other hand, at higher surface coverages (10%, tests 3 and 4) for the two cations investigated, Co^{2+} and Sb^{3+}, the situation changed rather dramatically when the surface coverage was increased. For Co^{2+} the sorption is not as complete as with lower surface coverage, but for Sb^{3+} the sorption % is higher, ca. 95% (= 9.44/9.97).

For Sb also the time dependence of the sorption reaction was studied by sampling the solution after 5, 15 and 30 minutes. The corresponding real sorption-% increased from 5.55 to 9.50 to 9.55%. Thus at least for Sb the sorption kinetics is rather slow with a high surface coverage, at difference to the hematite case discussed above.

6.2.3 Solution equilibria

The goal in sorption modelling was to figure out what kind of species exists in the studied systems when the sorption occurs and what the concentrations of the dominating species would be at the surface.

The first step in understanding the sorption behaviour of any cation is to find out in what form that cation may exist in the solution in the studied environment. Therefore we need to first investigate the solution equilibria for each studied cation type in order to find the dominating species. This can be done on the purely thermodynamic basis without any interaction with oxide surfaces.

At 280ºC the logarithm of the stability constant for the autoprotolysis reaction of water

$$H_2O = H^+ + OH^-, \qquad \log K_w \tag{17}$$

is equal to -11.24.

The speciation of Zn, Co, Ni and Sb in simulated PWR water has been calculated in Figure 15 using the equilibrium constants in
Table 5 (both at infinite dilution and corrected to 0.038 M ionic strength at 280 ºC) for the metal hydrolysis:

$$M^{2+} + nH_2O = M(OH)_n^{2-n} + nH^+, \qquad \log K_n^0 \tag{18}$$

from which the apparent equilibrium constant K_n^a including the activity correction is calculated as

$$\log K_n^0 = -\log\left\{\gamma_1^4\left[\mathrm{M}^{2+}\right]\right\} + \log\left\{\gamma_1^{(2-n)^2}\left[\mathrm{M(OH)}_n^{2-n}\right]\right\} + n\log\left\{\gamma_1\left[\mathrm{H}^+\right]\right\} \Rightarrow$$
$$\log K_n^a = \log K_n^0 + \left(3n - n^2\right)\log\gamma_1 = -\log\left[\mathrm{M}^{2+}\right] + \log\left[\mathrm{M(OH)}_n^{2-n}\right] + n\log\left[\mathrm{H}^+\right] \quad (19)$$

where the mass action equation for the reaction (18) is written out by concentrations and activity coefficients; log activity coefficients for ion of charge z, are assumed to be of the form $\log\gamma_z = z^2\log\gamma_1$, where γ_1 is the activity coefficient of unit charged ion.

For neutral Sb species

$$\mathrm{Sb(OH)_3} + n\mathrm{H_2O} = \mathrm{Sb(OH)}_{3+n}^{-n} + n\mathrm{H}^+, \qquad \log K_n^0 \quad (20)$$

from which the apparent equilibrium constant K_n^a is calculated as

$$\log K_n^0 = -\log\left[\mathrm{Sb(OH)_3}\right] + \log\left\{\gamma_1^{n^2}\left[Sb\mathrm{(OH)}_n^{-n}\right]\right\} + n\log\left\{\gamma_1\left[\mathrm{H}^+\right]\right\} \Rightarrow$$
$$\log K_n^a = \log K_n^0 - \left(n^2 + n\right)\log\gamma_1 = -\log\left[\mathrm{Sb(OH)_3}\right] + \log\left[Sb\mathrm{(OH)}_n^{-n}\right] + n\log\left[\mathrm{H}^+\right] \quad (21)$$

The activity coefficient was calculated by Davies equation at 280ºC and a value of -0.17 was applied for $\log\gamma_1$ in the calculation of apparent equilibrium constants listed in Table 5 (ionic strength 0.038 M).

The pH value at the experimental conditions was slightly over 8, where almost all studied elements except antimony are negatively charged triple hydroxides. Only small amount of antimony consist of negatively charged hydroxide and most of antimony is in neutral basic species $Sb(OH)_3$.

*Table 5. Equilibrium constants for the hydrolysis reactions of Co, Ni, Sb and Zn at 280ºC. The activity corrected values (marked in **bold**) were used in all Fiteql calculations.*

	Co^{2+} [16]		Ni^{2+} [15]		$Sb(OH)_3$ [19]		Zn^{2+} [14]	
n	$\log K_n^0$	$\log K_n^a$	$\log K_n^0$	$\log K_n^a$	$\log K_n^0$	$\log K_n^a$	$\log K_n^0$	$\log K_n^a$
-1	-	-	-	-	-0.673	**-0.673**	-	-
1	-5.87	**-6.21**	-6.42	**-6.76**	-10.01	**-9.67**	-4.4	**-4.74**
2	-12.13	**-12.47**	-13.59	**-13.93**	-	-	-9.73	**-10.07**
3	-19.74	**-19.74**	-18.48	**-18.48**	-	-	-18.17	**-18.17**

From the calculated speciation presented in Figure 15 it can be seen that in typical PWR conditions at especially $Sb(OH)_3$ is dominating, which differs strongly on the behaviour of other investigated cationic species. On the other hand, the stability region for $Zn(OH)_2$ seems also to be rather wide. This rather simple thermodynamic investigation shows that there are noticeable differences in the behaviour of different cationic species in studied system and therefore different surface complexation behaviour can also be expected.

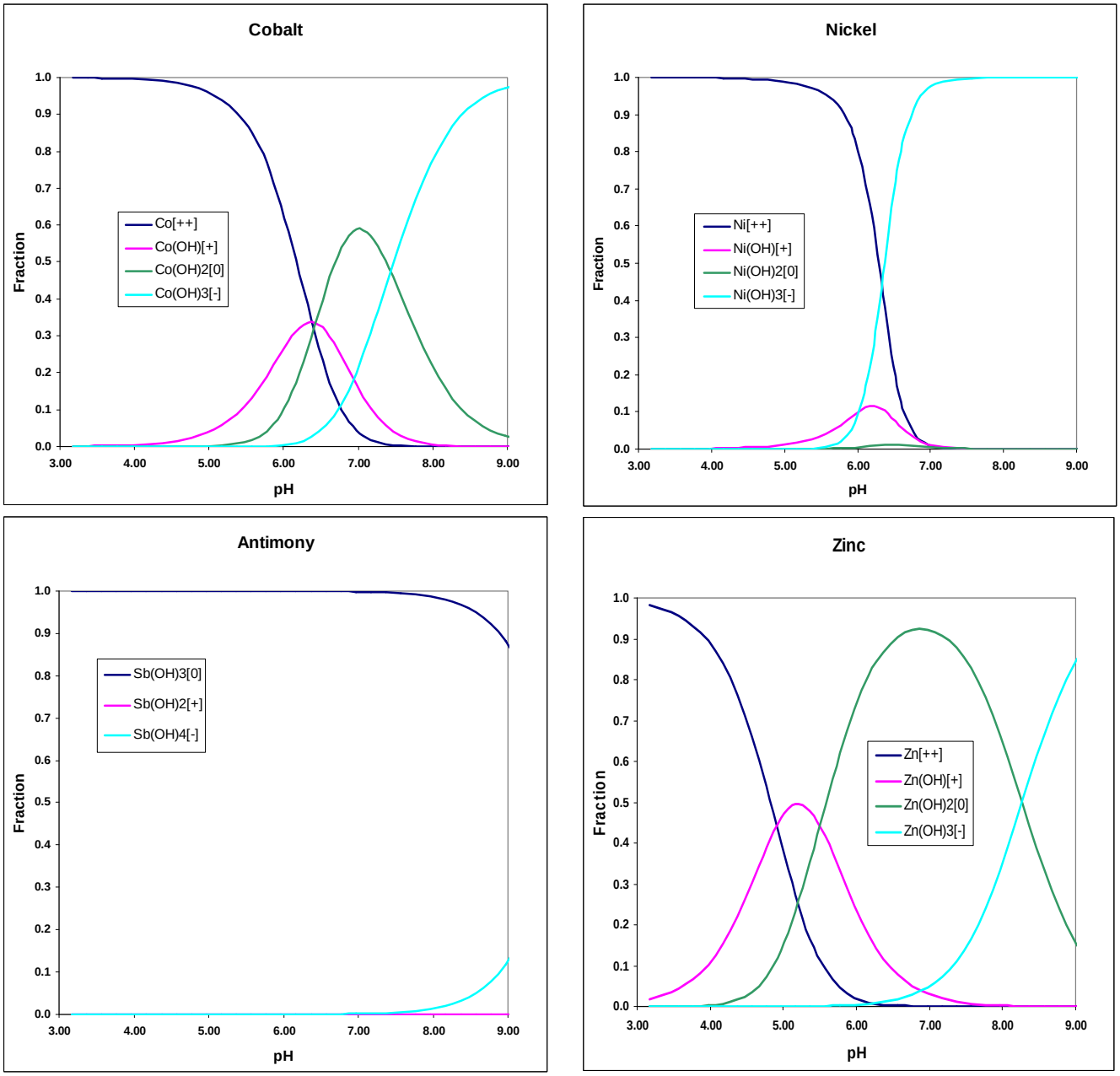

Figure 15 Speciation of Co(II), Ni(II), Sb(III) and Zn(II) in simulated PWR water conditions at 280 ºC.

6.2.4 Adsorption equilibrium

The next step in the study was to take the effects of oxide surfaces into account in estimating the high temperature behaviour of the studied cations in simulated PWR conditions. For optimizing the surface chemical equilibrium, FITEQL v. 4.0 has been used. The surface hydrolysis of magnetite is described in terms of the 1-pK surface complexation model in which a single surface protonation step is required, as applied in our earlier work for hematite surface [17]

$$\equiv \text{Fe-OH}^{1/2+} = \equiv \text{Fe-O}^{1/2-} + \text{H}^{+}, \qquad K_{\text{a}} \tag{22}$$

The mass-action equation for reaction (22) is given by

$$K_a = \frac{\left[\equiv \text{Fe-O}^{1/2-}\right] e^{-\frac{1}{2}F\psi/RT} \left[\text{H}^+\right]}{\left[\equiv \text{Fe-OH}^{1/2+}\right] e^{\frac{1}{2}F\psi/RT}} = \frac{\left[\equiv \text{Fe-O}^{1/2-}\right]\left[\text{H}^+\right] e^{-F\psi/RT}}{\left[\equiv \text{Fe-OH}^{1/2+}\right]} \tag{23}$$

where T is the temperature, R is the gas constant (8.314 J/K), F is the Faraday constant (96 485 C/mol), and ψ is the electrostatic potential at the interface (where the surface protons are located). Note that electrostatic correction belongs to the surface site and depends on the charge of the site. The actual value of the electrostatic potential depends on the chosen surface charging model, such as Diffuse Layer Model (DLM) or the Constant Capacitance Model (CCM).

The basic species for 1-pK model in our FITEQL applications is $\equiv \text{Fe-OH}^0_{1/2}$, by which both charged species in reaction (22) are written as (note that in FITEQL product will be on the left hand side)

$$\begin{aligned} \equiv \text{Fe-OH}^{1/2+} &= \equiv \text{Fe-OH}^0_{1/2} + \tfrac{1}{2}\text{H}^+, \qquad K_a \\ \equiv \text{Fe-O}^{1/2-} + \tfrac{1}{2}\text{H}^+ &= \equiv \text{Fe-OH}^0_{1/2}, \qquad K = 1 \end{aligned} \tag{24}$$

and the mass-action equations for above reactions are given by

$$\begin{aligned} K_a &= \frac{\left[\equiv \text{Fe-OH}^0_{1/2}\right]\left[\text{H}^+\right]^{\frac{1}{2}}}{\left[\equiv \text{Fe-OH}^{1/2+}\right] e^{\frac{1}{2}F\psi/RT}} \\ 1 &= \frac{\left[\equiv \text{Fe-OH}^0_{1/2}\right]}{\left[\equiv \text{Fe-O}^{1/2-}\right] e^{-\frac{1}{2}F\psi/RT} \left[\text{H}^+\right]^{\frac{1}{2}}} \end{aligned} \tag{25}$$

The total concentration of surface sites is calculated as the sum of neutral and charged species

$$\begin{aligned} T_{\text{Fe-OH}^{1/2}} &= \left[\equiv \text{Fe-OH}^0_{1/2}\right] + \left[\equiv \text{Fe-OH}^{1/2+}\right] + \left[\equiv \text{Fe-O}^{1/2-}\right] \\ &= \left[\equiv \text{Fe-OH}^0_{1/2}\right] \left\{ 1 + \frac{\left[\text{H}^+\right]^{\frac{1}{2}} e^{-\frac{1}{2}F\psi/RT}}{K_a} + \frac{1}{\left[\text{H}^+\right]^{\frac{1}{2}} e^{-\frac{1}{2}F\psi/RT}} \right\} \end{aligned} \tag{26}$$

The concentrations of different site types are, after some algebra, given by

$$\begin{aligned} \left[\equiv \text{Fe-H}^0_{1/2}\right] &= \frac{\left[\text{H}^+\right]^{\frac{1}{2}} e^{-\frac{1}{2}F\psi/RT}}{\left[\text{H}^+\right]^{\frac{1}{2}} e^{-\frac{1}{2}F\psi/RT} + \dfrac{\left[\text{H}^+\right] e^{-F\psi/RT}}{K_a} + 1} T_{\text{Fe-OH}^{1/2}} \\ \left[\equiv \text{Fe-OH}^{1/2+}\right] &= \frac{1}{K_a} \frac{\left[\text{H}^+\right] e^{-F\psi/RT}}{\left[\text{H}^+\right]^{\frac{1}{2}} e^{-\frac{1}{2}F\psi/RT} + \dfrac{\left[\text{H}^+\right] e^{-F\psi/RT}}{K_a} + 1} T_{\text{Fe-OH}^{1/2}} \\ \left[\equiv \text{Fe-O}^{1/2-}\right] &= \frac{1}{\left[\text{H}^+\right]^{\frac{1}{2}} e^{-\frac{1}{2}F\psi/RT} + \dfrac{\left[\text{H}^+\right] e^{-F\psi/RT}}{K_a} + 1} T_{\text{Fe-OH}^{1/2}} \end{aligned} \tag{27}$$

The surface charge density is given by

$$q_s = \frac{1}{2}\left\{\left[\equiv \text{Fe-OH}_2^{1/2+}\right] - \left[\equiv \text{Fe-O}^{1/2-}\right]\right\} = -\frac{T_{\text{Fe-OH}^{1/2}}}{2}\frac{K_a - \left[\text{H}^+\right]e^{-F\psi/RT}}{K_a\left(1+\left[\text{H}^+\right]^{\frac{1}{2}}e^{-\frac{1}{2}F\psi/RT}\right)+\left[\text{H}^+\right]e^{-F\psi/RT}} \quad (28)$$

Starting directly from the first equation of (22) and assuming that only positive and negative sites exist, a slightly different expression for the charge density is obtained

$$q_s = \frac{1}{2}\left\{\left[\equiv \text{Fe-OH}_2^{1/2+}\right] - \left[\equiv \text{Fe-O}^{1/2-}\right]\right\} = -\frac{T_{\text{Fe-OH}^{1/2}}}{2}\frac{K_a - \left[\text{H}^+\right]e^{-F\psi/RT}}{K_a + \left[\text{H}^+\right]e^{-F\psi/RT}} \quad (29)$$

The difference between these two approaches is biggest at very low pH values, where the proton concentration is high, but fortunately quite often the surface potential is also high and positive, and therefore the second term in the difference term (first bracket in denominator) is smaller than one.

The surface charge will, naturally be affected by the sorption of anions or cations onto the surface, but the basic method will be the same. However, there is a need to add, a phenomenological, dependence between the surface charge and potential. A few common approaches to express the dependence exist, but in the DLM applied in the calculations the dependence is given by

$$\sigma_s = a_s \rho q_s = -\frac{2\varepsilon\varepsilon_0\kappa RT}{F}\sinh\left(z\frac{F\psi}{2RT}\right)$$

where (30)

$$\kappa = 2\left(\frac{1000F^2I}{\varepsilon\varepsilon_0 RT}\right)^{\frac{1}{2}}$$

where κ is the Debye-Hückel parameter (inverse thickness of the diffuse layer), as is the specific surface area of the adsorbent, ρ is the density of the adsorbent, ε is the relative permittivity, ε_0 is the vacuum permittivity, and I is the stoichiometric ionic strength.

The surface complexation models tested for magnetite were the DLM and CCM. The DLM gave a slightly better fit, and therefore it was applied in cation sorption studies (both for now titrated magnetite and earlier titrated hematite) together with the non-electrostatic model (NEM) for which all electrostatic effects are omitted. A single surface complexation model of the form,

$$\equiv \text{Fe-O}^{1/2-} + \text{M}^{2+} + \text{H}_2\text{O} = \equiv \text{Fe-M}^{1/2+}\left(\text{OH}\right) + \text{H}^+, \qquad K_{\text{M}}^{'} \quad (31)$$

or employing neutral component species

$$\equiv \text{Fe-OM}\left(\text{OH}\right)^{1/2+} + \tfrac{3}{2}\text{H}^+ = \equiv \text{Fe-OH}_{1/2}^0 + \text{M}^{2+} + \text{H}_2\text{O}, \qquad K_{\text{M}} \quad (32)$$

was fitted to the experimental systems. The hydroxyl sorbed species was chosen due to high pH range studied. In order to get more information about the surface reaction a much wider pH-range should be studied.

6.2.5 Modelling results

Both hematite and magnetite surfaces were studied and basic modelling parameters obtained in our earlier or present study, or from literature are collected in Table 6. Magnetite titrations were successfully fitted, although fitting is not perfect and needed the assumption on ionic strength of 0.1 M during titrations. The fitted surface site densities were near the values estimated by the Gran method. The measured and calculated surface charges are shown in Figure 16. The measured surface charge is obtained from the high temperature titrations as the amount of free protons left in the solution during the titration and the surface properties of the oxides are known.

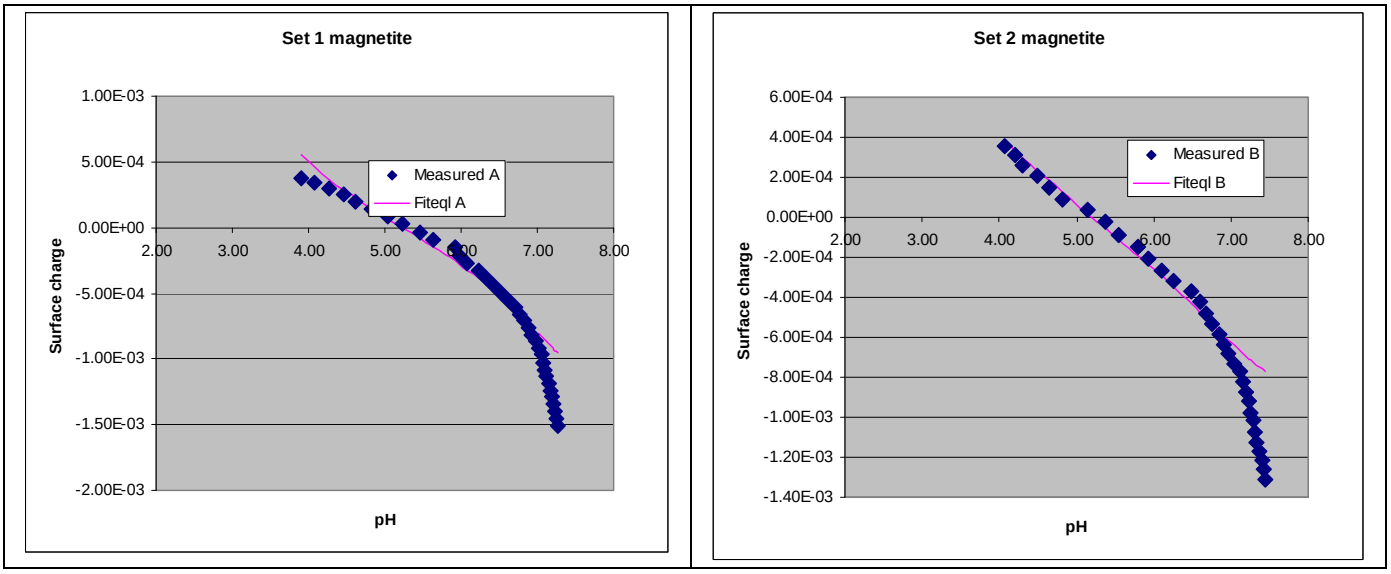

Figure 16. Measured and calculated surface charges for the two titrations of magnetite.

Table 6. Basic modelling parameters for sorption on hematite and magnetite.

	Hematite	Magnetite
Specific surface area (m^2/g)	8.3	40
Site density (µmol/g)	0.75	70
Concentration of oxide used in batch experiments (g/L)	50	10
pH of zero net proton charge	4.7	5.4

Fitted binding constants for both magnetite and hematite and are given in Table 7. For the sake of comparison also the stability constants for the adsorption on hematite in simulated BWR conditions from a previous work [17] have been included in Table 8. The surface complexation reactions in BWR conditions has been

$$2\ (\equiv SOH_{½}^{\circ}) + m\ M^{2+} + n\ H_2O \Leftrightarrow (\equiv SO)_2M_m(OH)_n^{2m-(n+1)} + (n+1)\ H^+, \quad \log K_M \qquad (33)$$

where m = 1 or 2 and n = 0, 1, 2, etc. As can be seen from the calculated values the stability constants in the two environments vary quite much from each other. But it is worth mentioning that the environment has been different. Also the modelling approach differed slightly.

Table 7. Fitted stability constants. (log K)(Experiment 1 and 2 are CCM and DLM).

Magnetite	Co^{2+}	Ni^{2+}	$Sb(OH)_3$	Zn^{2+}
Experiment 1	-0.53	2.08	2.21	1.62
Experiment 2	-0.51	-	3.60	-
Hematite				
Experiment 1	2.3	4.0	6.0	4.1

Table 8. Optimized DLM stability constants for reaction surface complexation reactions on hematite in simulated BWR conditions [17].

	log K		
n	**Zn**[a]	**Ni**[a]	**Co**[b]
3	5.18	1.61	
5	-0.23	-5.99	5.37
[a] Monodentate reaction (m = 1), [b] Bidentate reaction (m = 2)			

The calculated sorption percentages together with the experimental results are shown in Figure 17. From the figure it can be seen that for Zn and Co the sorption percentage is high in a wide pH region whereas for Ni and Sb the sorptivity increases above neutral pH (i.e. 5.6 at 280°C). The experimental points have been used as fitting points through which the fitted curve should pass. All in all, the sorption calculations in simulated PWR conditions have turned out to be more complex than expected. One of the problems in calculating the sorption trends for different species has been that only few data on parameters at relevant temperature and pH for different cations can be found in data bases. This has been a noticeable problem especially in calculating parameter values for Sb. Therefore the proposed modelling approach needs more refinement that is underway. Also the number of the experimental points needs to be larger for the proposed approach.

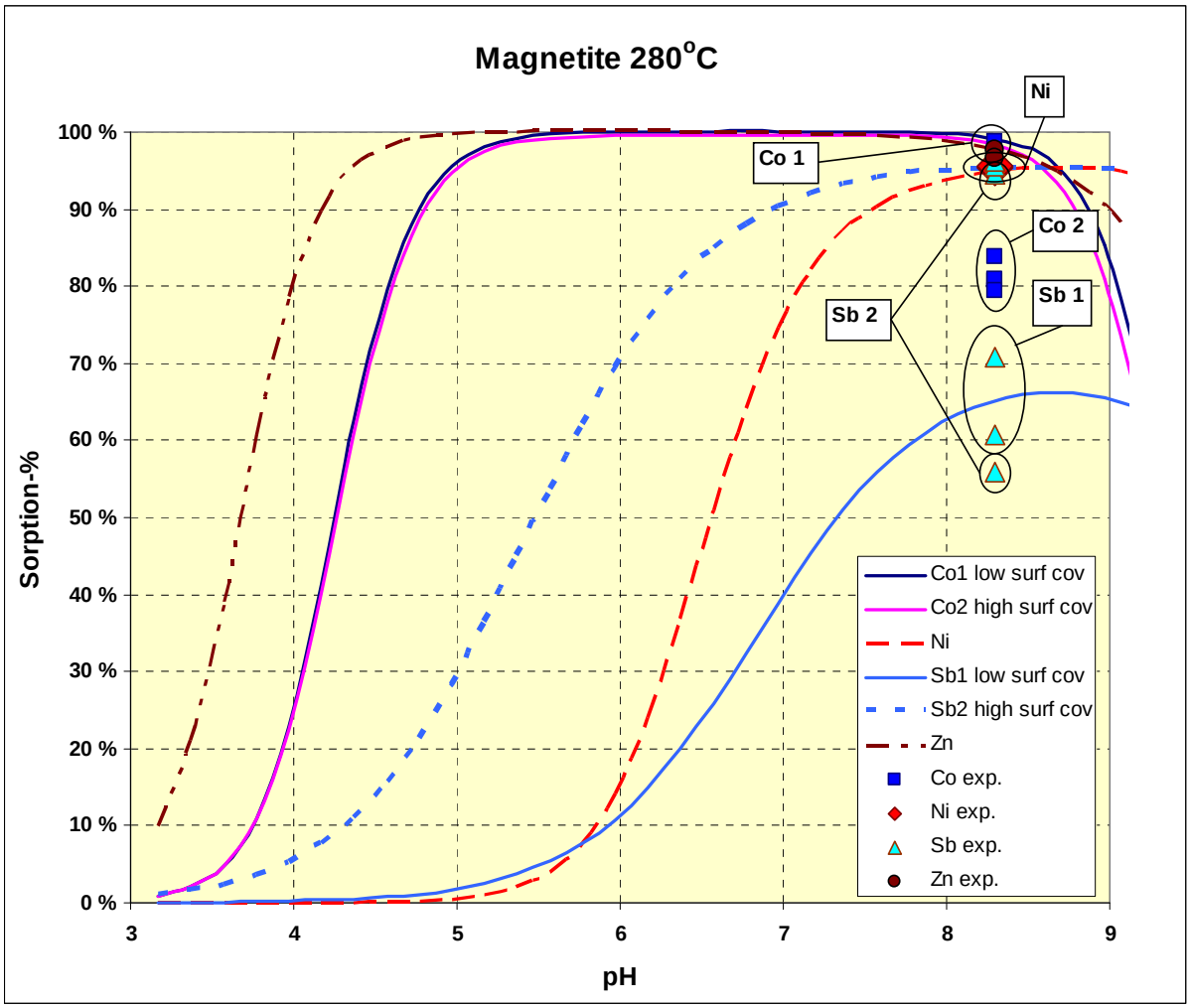

Figure 17. Experimental sorption results different cations and calculated sorption behaviour for magnetite surfaces at simulated PWR conditions. All experiments were carried out at pH=8.3. Co1 and Co2 as well as Sb1 and Sb2 are results for measurements with theoretical different surfaces coverages.

The surface potential is one of the direct outputs in FITEQL; the dependence of the surface potential as a function of pH is given in Figure 16. At the studied temperature, 280 ºC, the thermal energy E_{thermal} is equal to 46 meV, and therefore, the electrostatic corrections of the form $e^{-\frac{e\psi}{E_{\text{thermal}}}}$, are high, over one in logarithmic scale.

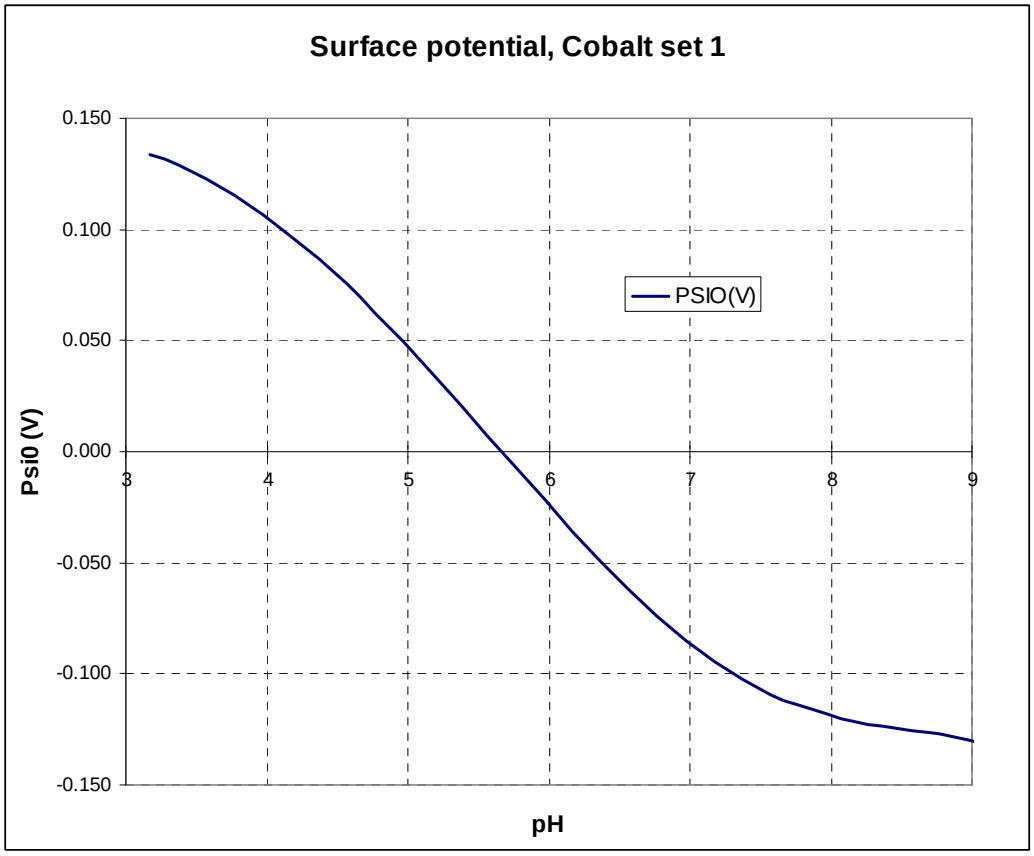

Figure 18. Modelled surface potential as a function of pH in the case of first Co experiment. For both low and high pH values the Coulombic term for activity correction is over one log unit, for ions of unit charge.

7 Validation of results

Estimates for the rate constants and diffusion coefficients of individual metallic constituents of the inner layer, as well as the apparent diffusion coefficients during outer layer growth were estimated by a quantitative comparison of the in-situ EIS and ex-situ XPS depth profile data with the model equations outlined above.

The calculated curves (solid lines in Figure 2, Figure 3 and Figure 8) are in good agreement with the experimental data (points), indicating that the model is once again able to account for the essential features of the data. Sensitivity analyses performed in our previous paper [1] by estimating the effect of a 10% change of the respective kinetic parameters on the calculated depth profiles have demonstrated that the obtained values are significant and can be used to explore further the transport mechanism through the oxide.

The estimates of the stability constants of the surface complexes of Co, Ni, Zn and Sb on hematite and magnetite have been obtained by fitting the experimentally derived surface charges to the equations of several electrostatic model approaches. Examples of the goodness of fit are shown in Figure 16 and demonstrate the ability of these approaches to successfully account for the experimental data.

8 Conclusions

The experimental and calculational results obtained in the present paper have clearly indicated the significant effect of Zn injection in simulated high-temperature PWR water on the initial

stages of the growth and restructuring of the oxide film on AISI 316L(NG). In unbuffered PWR water, a drastic decrease of the thickness of the oxide is observed after Zn injection. This is demonstrated to be due to both the change in the pH of the electrolyte as a result of Zn hydrolysis reactions and the Zn adsorption on/incorporation in the oxide film which leads to significant decrease of the rates of ion transport in the inner layer and the interfacial reactions at the inner layer/electrolyte interface. On the other hand, the effect of Zn on film growth and restructuring in buffered PWR water is much less dramatic, but still significant. This effect is demonstrated to be due to both Zn incorporation in the inner layer and the probable formation of a new Zn-rich phase as the outer layer.

These findings have been quantified in terms of estimates for the reaction rate constants at the alloy/inner layer and inner layer/electrolyte interfaces, as well as diffusion coefficients for the solid-state transport in the inner layer, all calculated for the individual metallic constituents. The rates of outer layer formation have been also estimated on the basis of a formal model that treats the growth of its crystallites as a process of transport of individual metallic constituents characterised by their apparent diffusion coefficients.

The surface complexation studies indicate that Zn and Co species are sorpted more strongly onto the oxide surfaces than Ni and Sb at a wide pH scale. The experiments showed that Ni is sorpted noticeably less on hematite surfaces than the other cations in the simulated PWR environment. On magnetite the sorption tendency seems to be the lowest for Sb at low surface coverages, but when the surface coverage increases also the sorption tendency of Sb seems to increase to over 90%. Furthermore, both thermodynamic solution equilibrium calculations and surface complexation studies have shown that the behaviour of Sb in simulated PWR conditions is rather different from that of other studied cations.

9 Summary

The oxidation of AISI 316L(NG) stainless steel in simulated Pressurised Water Reactor (PWR) coolant with or without addition of 1 ppm Zn at 280°C for up to 96 h has been characterised in-situ by Electrochemical Impedance Spectroscopy (EIS), both at the corrosion potential and under anodic polarisation up to 0.5 V vs. the reversible hydrogen electrode (RHE). Additional tests were performed in simulated PWR coolant with the addition of 0.01 M $Na_2B_4O_7$ to exclude the effect of pH excursions probably due to Zn hydrolysis reactions. The thickness and in-depth composition of the oxide films formed at open circuit and at 0.5 V vs. RHE in the investigated electrolytes have been estimated from X-ray photoelectron spectroscopy (XPS) depth profiles. The kinetic and transport parameters characterising the oxide layer growth have been estimated using a calculational procedure based on the Mixed Conduction Model for oxide films. Successful simulations of both the EIS and XPS data have been obtained using the proposed procedure. The parameter estimates are discussed in terms of the effect of Zn on the growth and restructuring of the oxide layers on stainless steel in LWR conditions. In addition, sorption tests were employed to quantitatively estimate the adsorption of a range of aquoions (Co, Ni, Zn, and Sb) on hematite and magnetite type oxides. This was accomplished by measuring the solution concentrations before and after the sorption. Some data on the kinetics of sorption of Sb have been also obtained. The surface site density on both oxides was determined by the Gran method both at ambient temperature and at 280 ºC. The results were interpreted by using the 1-pK approach of the surface complexation model, and the electrostatic effects were taken into account by employing a constant capacitance or diffuse layer models. Stability constants of surface complexes of Co, Ni, Zn and Sb on magnetite and hematite oxides have been estimated and discussed.

10 Nomenclature

b_c	exponential coefficient of the reaction of consumption of point defects, V^{-1}
b_{redox}	exponential coefficient of the redox reaction at the inner layer/electrolyte interface, V^{-1}
$c_{Zn,aq}$	concentration of Zn in the electrolyte, mol cm^{-3}
c_t	concentration of the titrant (NaOH), mol dm^{-3}
C	space charge layer capacitance, F cm^{-2}
$C_{F/E}$	capacitance at the inner layer/electrolyte interface, F cm^{-2}
D_{Cr}	diffusion coefficient of Cr in the inner layer, $cm^2\ s^{-1}$
$D_{Cr,OL}$	apparent diffusion coefficient of Cr in the outer layer, $cm^2\ s^{-1}$
D_e	diffusion coefficient of electronic current carriers in the inner layer, $cm^2\ s^{-1}$
D_{Fe}	diffusion coefficient of Fe in the inner layer, $cm^2\ s^{-1}$
$D_{Fe,OL}$	apparent diffusion coefficient of Fe in the outer layer, $cm^2\ s^{-1}$
D_i	diffusion coefficient of point defects in the inner layer, $cm^2\ s^{-1}$
D_{Ni}	diffusion coefficient of Ni in the inner layer, $cm^2\ s^{-1}$
$D_{Ni,OL}$	apparent diffusion coefficient of Ni in the outer layer, $cm^2\ s^{-1}$
D_{Zn}	diffusion coefficient of Zn in the inner layer, $cm^2\ s^{-1}$
$D_{Zn,OL}$	apparent diffusion coefficient of Zn in the outer layer, $cm^2\ s^{-1}$
E	applied potential, V
$\vec{E}$	field strength in the inner layer, V cm^{-1}
$E_{o,H}$	apparatus constant, mV
E_j	liquid junction potential depending on ionic strength and free hydrogen ion concentration, mV
$E_{thermal}$	thermal energy, eV
F	Faraday number, 96487 C mol^{-1}

H_o	amount of excess protons in the beginning of the titration, mol dm^{-3}
I	ionic strength, mol kg^{-1}
$k_{g,Cr}$	rate constant of oxidation of Cr at the alloy/inner layer interface, cm^4 mol^{-1} s^{-1}
$k_{g,Fe}$	rate constant of oxidation of Fe at the alloy/inner layer interface, cm^4 mol^{-1} s^{-1}
$k_{g,Ni}$	rate constant of oxidation of Ni at the alloy/inner layer interface, cm^4 mol^{-1} s^{-1}
$k_{c,Cr}$	rate constant of dissolution of Cr at the inner layer/electrolyte interface, cm s^{-1}
$k_{c,Fe}$	rate constant of oxidation of Fe at the inner layer/electrolyte interface, cm s^{-1}
$k_{c,Ni}$	rate constant of oxidation of Ni at the inner layer/electrolyte interface, cm s^{-1}
k_{redox}	rate constant of the redox reaction at the inner layer/electrolyte interface, mol cm^{-2} s^{-1}
K_a	equilibrium constant for surface protonation
K_{enr}	enrichment factor of Zn at the inner layer/electrolyte interface
K_n^0	equilibrium constant for metal hydrolysis
K_M	equilibrium constant for surface complexation reaction
K_n^a	apparent equilibrium constant for metal hydrolysis including the activity correction
K_w	autoprotolysis constant of water
L	inner layer thickness, cm
q_s	surface charge density
R	universal gas constant, 8.314 J mol^{-1} K^{-1}
$R_{F/E}$	charge transfer resistance at the inner layer/electrolyte interface, Ω cm^2
T	temperature, K
$T_{Fe\text{-}OH½}$	total concentration of surface sites, mol dm^{-3}
V_{beg}	solution volume of the titrated solution before titration, dm^{-3}
V_{ef}	equivalent volume of the titrant, dm^{-3}
$V_{m,MO}$	molar volume of the phase in the inner layer, cm^3 mol^{-1}
V_t	added volume of the titrant, dm^{-3}
X	formal valency state of Fe in the inner layer
y_{Cr}	mass fraction of Cr in the oxide normalised to the total mass fraction of cations
y_{Fe}	mass fraction of Fe in the oxide normalised to the total mass fraction of cations
y_{Ni}	mass fraction of Ni in the oxide normalised to the total mass fraction of cations
y_{Zn}	mass fraction of Zn in the oxide normalised to the total mass fraction of cations
z	charge number
Z	overall impedance, Ω cm^2
Z_e	impedance due to the electronic properties of the inner layer, Ω cm^2
Z_f	inner layer impedance, Ω cm^2
$Z_{F/E}$	impedance of the inner layer/electrolyte interface, Ω cm^2
Z_i	impedance due to point defect transport in the inner layer, Ω cm^2
α	polarisability of the inner layer/electrolyte interface
ε	dielectric constant of the inner layer of oxide or the relative permittivity
ε_0	dielectric permittivity of free space, 8.85×10^{-14} F cm^{-1} or the vacuum permittivity
γ	activity coefficient
σ_s	surface potential, V
ψ	electrostatic potential at the oxide/solution interface, V
κ	Debye-Hückel parameter, m^{-1}
ρ	density of the adsorbent, kg m^{-3}

References

1. I. Betova, M. Bojinov, P. Kinnunen, K. Lundgren, T. Saario, J. Electrochem. Soc. 155 (2008) C81-C92.
2. M. Bojinov, P. Kinnunen, V. Lehtovuori, T. Saario, A conceptual four-layer model of the oxide layer on structural materials in LWRs with emphasis on the oxide coolant interactions, *VTT Research Report TUO75-056405*, VTT 2006, 25 p.
3. G. Gran, Determination of the equivalence point in potentiometric titrations. Part ll. Analyst, 77(1952) 661.
4. M. Bojinov, P. Kinnunen, K. Lundgren, G. Wikmark, J. Electrochem.Soc. 152 (2005) B250.
5. M. Bojinov, A. Galtayries, P. Kinnunen, A. Machet, P. Marcus, Electrochim. Acta 52(2007) 7475.
6. B. Beverskog, in Proc. International Conference "Water Chemistry of Nuclear Reactor Systems", San Francisco, CA, October 10-14, 2004, paper 2.7 (CD-ROM publication).
7. Y. Takeda, T. Shoji, M. Bojinov, P. Kinnunen, T. Saario, Appl. Surf. Sci. 252(2006) 8580.
8. S.E. Ziemniak, M. Hanson, Corros. Sci. 44 (2002) 2209.
9. R.L. Tapping, R.D. Davidson, E. McAlpine, D.H. Lister, Corros. Sci. 26 (1986) 563.
10. D.H. Lister, E. McAlpine, and R.D. Davidson, Corros. Sci. 27 (1987)113.
11. Z. Szklarska-Smialowska, K. Chou, Z. Xia, Corros. Sci. 32 (1992) 609.
12. V. Philippini, Au. Naveau, H. Catalette, S. Leclercq, J. Nucl. Mat. 348 (2006) 60-69.
13. T. Missana, M. García-Gutíerrez, V. Fernandez, Geochimica et Cosmochimica Acta, 67, No. 14 (2003) 2543–2550
14. P. Bénézeth, D. A. Palmer, D. J. Wesolowski, C. Xiao, J. Solution Chem., 31 (2002) 947–973.
15. S. E. Ziemniak, M. A. Goyette, J. Solution Chem., 33 (2004) 1135–1159
16. S. E. Ziemniak, M. A. Goyette, K. E. S. Combs, J. Solution Chem., 28 (1999) 809–836
17. I. Betova, M. Bojinov, P. Kinnunen, J. Lehikoinen, K. Lundgren, T. Saario, Proceedings of ICAPP'07, Nice, France, 2007, paper No. 7122.
18. T. W. Wolery, R. L Jarek. Software User's Manual EQ3/6, Version 8.0, (2003). Report 10813-UM-8.0-00, Sandia National Laboratories, Albuquerque, New Mexico, USA.

Report's title	
ANTIOXI - Incorporation of coolant originating cations into the oxide films on stainless steels - experiments and modelling	
Customer, contact person, address EC / Marc Deffrennes, Commission européenne, Rue du Champ de Mars 21, B- 1050 Brussels, Belgium	Order reference
Project name ANTIOXI	Project number/Short name 6402 ANTIOXI
Author(s) Martin Bojinov, Petri Kinnunen, Markus Olin	Pages 39
Keywords oxide film, hematite, magnetite Zn, PWR, stainless steel, sorption	Report identification code VTT-R-10851-07

Summary

The oxidation of AISI 316L(NG) stainless steel in simulated Pressurised Water Reactor (PWR) coolant with or without addition of 1 ppm Zn at 280°C for up to 96 h has been characterised in-situ by Electrochemical Impedance Spectroscopy (EIS). Additional tests were performed in simulated PWR coolant with the addition of 0.01 M $Na_2B_4O_7$ to exclude the effect of pH excursions probably due to Zn hydrolysis reactions. The thickness and in-depth composition of the oxide films formed at open circuit and at 0.5 V vs. RHE in the investigated electrolytes have been estimated from X-ray photoelectron spectroscopy (XPS) depth profiles. The kinetic and transport parameters characterising the oxide layer growth have been estimated using a calculation procedure based on the Mixed Conduction Model for oxide films. Successful simulations of both the EIS and XPS data have been obtained using the proposed procedure. The parameter estimates are discussed in terms of the effect of Zn on the growth and restructuring of the oxide layers on stainless steel in LWR conditions.

In addition, sorption tests were employed to quantitatively estimate the adsorption of a range of aquoions (Co, Ni, Zn, and Sb) on hematite and magnetite type oxides. This was accomplished by measuring the solution concentrations before and after the sorption. Some data on the kinetics of sorption of Sb have been also obtained. The surface site density on both oxides was determined by the Gran method both at ambient temperature and at 280 °C. The results were interpreted by using the 1-pK approach of the surface complexation model, and the electrostatic effects were taken into account by employing a constant capacitance or diffuse layer models. Stability constants of surface complexes of Co, Ni, Zn and Sb on magnetite and hematite oxides have been estimated and discussed.

Confidentiality	Public

Espoo 12.3.2008

Signatures	Signatures
Accepted by Liisa Heikinheimo Technology Manager	Written by Petri Kinnunen, Senior Research Scientist, Coordinator

VTT's contact address
P.O.Box 1000, 02044 VTT, Finland

Distribution (customer and VTT)

European Commission 1 original
VTT 1 original
BGH2 Society 1 original